https://doi.org/10.5194/egusphere-2026-5128
Preprint. Discussion started: 29 September 2026

Aerosol Modulation of Warm Sector Extreme Rainfall over Coastal South China in Its Multi-Scale Structures: Progressive Impact Chain Extension from Microphysics to Convective Organization

Nuofeng Tan[1], Pengguo Zhao[1], Hui Xiao[2], and Chuanhong Zhao[1]

[1]Climate Change and Resource Utilization in Complex Terrain Regions Key Laboratory of Sichuan Province, Chengdu Plain Urban Meteorology and Environment Observation and Research Station of Sichuan Province, Sichuan Provincial Engineering Research Center for Meteorological Disaster Prediction and Early Warning, School of Atmospheric Sciences, Chengdu University of Information Technology, Chengdu 610225, China
[2]Guangzhou Institute of Tropical and Marine Meteorology, China Meteorological Administration, Guangzhou 510640, China

Correspondence to: Pengguo Zhao (zpg@cuit.edu.cn); Hui Xiao (xh_8646@163.com)

Abstract. How aerosols modulate warm-sector extreme rainfall over South China by altering mesoscale convective system (MCS) organization remains poorly understood. We investigate a coastal warm-sector extreme-rainfall event on 10–11 May 2022 using five WRF v4.3.3 sensitivity experiments with different water-friendly aerosol concentrations. Multiscale responses are diagnosed using a two-dimensional discrete cosine transform, hydrometeor mass budgets, and buoyancy analysis. All experiments reproduce the inland frontal and coastal warm-sector rainbands, while aerosol sensitivity is concentrated in coastal MCS continuity, convective-scale hydrometeor activity, and rainwater production. As aerosol loading increases from low to moderate levels, condensational growth and cloud-water collection by raindrops intensify, establishing a more persistent warm-rain water source. Increased supercooled cloud water further promotes snow and graupel riming and melting, strengthening cold-rain processes. Meanwhile, low-level inflow, ascent, and hydrometeor columns become better aligned, favoring sustained MCS regeneration and a more continuous coastal rainband. At higher aerosol loading, smaller mean cloud droplet sizes suppress warm-rain production, while evaporative cooling and low-level cold anomalies intensify, coinciding with greater spatial separation of newly triggered convection from the primary rainband and increased rainband fragmentation. Although cold-rain compensation occurs in a few intense cores late in the highest-concentration experiment, it does not restore regionally averaged rainwater generation or rainband continuity. These results reveal a non-monotonic aerosol sensitivity in which precipitation depends not only on local microphysical enhancement but also on whether microphysical and dynamical responses remain spatially coupled to the MCS regeneration zone within this coastal warm-sector convective system over South China.

Keywords: warm-sector extreme rainfall; South China; aerosol–cloud–precipitation interactions; mesoscale convective system; Multi-Scale Structures

https://doi.org/10.5194/egusphere-2026-5128
Preprint. Discussion started: 29 September 2026

1 Introduction

Atmospheric aerosols can modify atmospheric stability and the surface energy budget by scattering and absorbing radiation. They can additionally serve as cloud condensation nuclei(CCN) and ice-nucleating particles, and thus influence droplet activation, phase transitions, and precipitation-particle growth. These perturbations can propagate from microscopic particle properties to cloud optical properties, lifetimes, precipitation efficiency, and the water cycle at larger scales (Twomey, 1977; Albrecht, 1989; Rosenfeld et al., 2008). Through the microphysical pathway, higher aerosol loading generally raises cloud droplet number concentration, decreases mean droplet size, and modifies condensation, collision–coalescence, supercooled-water transport, and ice-phase growth. Through the radiative pathway, aerosols and aerosol-induced changes in cloud properties can reshape the thermodynamic environment. The two pathways may operate simultaneously and produce different responses in local convection, cloud clusters, and mesoscale convective systems (MCSs) (Stier et al., 2024; Bei et al., 2025). Aerosol microphysical effects do not lead to a universal enhancement or suppression of convection; their net effects vary with environmental setting and storm structure. Important environmental controls include humidity, instability, vertical wind shear, cloud-base height, and the location of dry layers. Recent case-based simulations further indicate that the precipitation response to CCN perturbations can vary among convective cases and can depend on wind shear and the simulation period (Tonn et al., 2025). These factors govern water-vapor supply to condensation and the lofting of supercooled liquid water above the freezing level. They also determine whether evaporative cooling can generate cold pools capable of triggering subsequent convection (Rosenfeld et al., 2008; Grant and van den Heever, 2015; Grabowski and Morrison, 2021). In-cloud entrainment, hydrometeor loading, the partitioning between warm- and cold-phase processes, updraft structure, and life cycle stage also shape the net response. If inference is based only on correlations between aerosols and cloud-top height, radar reflectivity, or rainfall intensity, environmental covariability may be misinterpreted as a causal aerosol effect (Varble, 2018; Igel and van den Heever, 2021; Varble et al., 2023). Microphysics, dynamics, and organizational structure should therefore be evaluated together within a shared environmental background.

Convective systems exhibit structure-dependent responses to aerosol perturbations. For isolated deep convection, aerosols may strengthen some updrafts by delaying warm rain and increasing supercooled cloud water and latent-heat release, but the response remains constrained by moisture, entrainment, hydrometeor loading, and precipitation evaporation (Storer et al., 2010; Li et al., 2011; Marinescu et al., 2021). The same case can yield divergent responses across models, indicating that microphysical parameterizations and their dynamical coupling are important sources of uncertainty (Zhang et al., 2021). Simulations of South China squall lines further indicate that aerosol perturbations may either reduce total precipitation or yield a modest increase, with the magnitude controlled by moisture supply and convective stage (Xiao et al., 2023). Thus, the “aerosol invigoration” mechanism inferred from a single cloud or a local intense core cannot be transferred directly to an organized convective system.

An MCS contains convective cores, stratiform precipitation regions, cold pools, low-level inflow, and mesoscale circulations. Its persistence relies on convective-cell initiation, merger, propagation, and regeneration, making it inherently multiscale

https://doi.org/10.5194/egusphere-2026-5128
Preprint. Discussion started: 29 September 2026

(Houze, 2004). Local aerosol-driven changes can displace triggering locations via evaporative cooling and cold-pool outflow, and may also reorganize convective and stratiform regions through latent-heat release, hydrometeor transport, and adjustments in updrafts; stronger local convection need not produce greater system-integrated precipitation. Previous studies show that wind shear can alter the updraft response of MCSs (Chen et al., 2020), compensation among internal microphysical pathways can weaken net precipitation changes (Lee and Feingold, 2010), and enhanced peripheral convection in tropical cyclones can coexist with a weakened storm core (Khain et al., 2010). This motivates separating convective-scale intense cores, intermediate-scale rainbands or clusters, and the system-scale background, and assessing whether cross-scale responses reinforce or compensate for one another.

Warm-sector heavy rainfall in South China's pre-summer rainy season provides a useful setting for these questions. These events typically develop in warm, moist air south of a front, and their intensity and location reflect the combined influence of low-level jets, moisture transport, coastal convergence, orographic lifting, and repeated MCS regeneration (Luo et al., 2020). Deep warm-cloud layers and abundant moisture favor condensation, collision–coalescence, and rapid warm-rain production through raindrop collection of cloud water, while supercooled cloud water together with snow and graupel growth and melting in deep convection keeps cold-rain processes important (Gao et al., 2021). Regional simulations indicate that precipitation over coastal South China can respond nonlinearly to aerosol perturbations (Wang et al., 2023). However, previous work has emphasized accumulated precipitation, peak rainfall intensity, and regional means, while giving less attention to whether aerosols alter the large-scale rainband structure or multiscale hydrometeor activity and convective regeneration within an MCS. An integrated diagnosis of how warm-rain, cold-rain, and cold-pool feedbacks evolve over the life cycle is also lacking.

We analyze a coastal South China warm-sector extreme-rainfall event on 10–11 May 2022 and use five water-friendly aerosol sensitivity experiments with WRF and Thompson aerosol-aware microphysics. With initial and boundary conditions and physics held fixed, a two-dimensional discrete cosine transform separates system-, intermediate-, and convective-scale hydrometeor signals. The scale decomposition is combined with hydrometeor mass budgets, buoyancy components, and tracking of intermediate-scale convective elements to assess how aerosol perturbations affect precipitation generation and organizational evolution in the coastal MCS. We address three questions: whether responses are consistent across scales; how the establishment of warm rain and amplification by cold rain jointly control system precipitation; and whether, under high aerosol concentrations, changes in evaporative cooling, cold-pool outflow, and triggering location can explain the transition of the rainband from continuous to discrete. By jointly considering microphysical efficiency, dynamical feedbacks, and multiscale organization, we characterize the non-monotonic aerosol response of warm-sector MCSs.

https://doi.org/10.5194/egusphere-2026-5128
Preprint. Discussion started: 29 September 2026

2 Methods

2.1 Case overview

On 10 May 2022, Guangdong lay along the northwestern flank of the western North Pacific subtropical high and in advance of a 500 hPa westerly trough. At 850 hPa, a northeast–southwest oriented shear line separated northerly flow on its northern side from strong warm, moist southwesterlies farther south, producing pronounced horizontal wind shear. At the surface, the front lay over northern Guangdong, whereas the coast and adjacent waters were controlled by a low-level southerly jet, with a wind-convergence zone near the coastline (Fig. S1). Air with high pseudoequivalent potential temperature converged along the coast and was lifted by topography, favoring MCS initiation and persistence.

The precipitation field featured two distinct rainbands. Inland northern Guangdong hosted a frontal rainband associated with the low-level shear line and southward-moving front, while a warm-sector rainband along the western Guangdong coast persisted under the combined influence of the low-level jet and coastal convergence. The two rainbands lay about 100 km apart, and both contained heavy-rain centers exceeding 250 mm. The maximum accumulations in the inland and coastal rainbands were 446.9 and 433.3 mm, respectively. The coastal warm-sector rainband occurred mainly from 15:00 UTC 10 May to 06:00 UTC 11 May, with a maximum hourly rainfall rate of 95.7 mm h^{-1} at 23:00 UTC 10 May. Radar observations and earlier analyses indicate that convective cloud clusters repeatedly formed and merged along the coast before propagating downstream, eventually forming linear MCSs with a training effect. The low-level jet, moisture transport, local topography, and coastal convergence jointly supported this evolution.

Xia et al. (2023) and Xiao et al. (2025) have documented in detail the low-level moisture transport, boundary-layer convergence, double-rainband structure, and microphysical characteristics of this event. Rather than revisiting the full event attribution, we focus on the coastal warm-sector heavy-rainfall period from 18:00 UTC 10 May to 12:00 UTC 11 May. Scale separation and atmospheric-column hydrometeor mass budgets are applied to compare hydrometeor distributions under different aerosol concentrations and to diagnose how MCS microphysical and dynamical processes change accordingly.

2.2 Model configuration and experimental design

The numerical experiments were conducted with WRF v4.3.3. Initial and boundary conditions are provided by ERA5, the fifth-generation ECMWF reanalysis (Hersbach et al., 2020), at 1 h temporal and 0.25° × 0.25° horizontal resolution.

Three two-way nested domains are configured at horizontal grid spacings of 9, 3, and 1 km, with time steps of 27, 9, and 3 s, and domain dimensions of 301 × 301, 391 × 391, and 421 × 421. The domain center is 22.0° N, 113.0° E. The model uses a Lambert projection with standard parallels at 15° N and 30° N (Fig. 1). The integration runs from 12:00 UTC 9 May 2022 to 12:00 UTC 11 May 2022, spanning 48 h. The vertical grid comprises 57 terrain-following levels capped at 50 hPa.

https://doi.org/10.5194/egusphere-2026-5128
Preprint. Discussion started: 29 September 2026

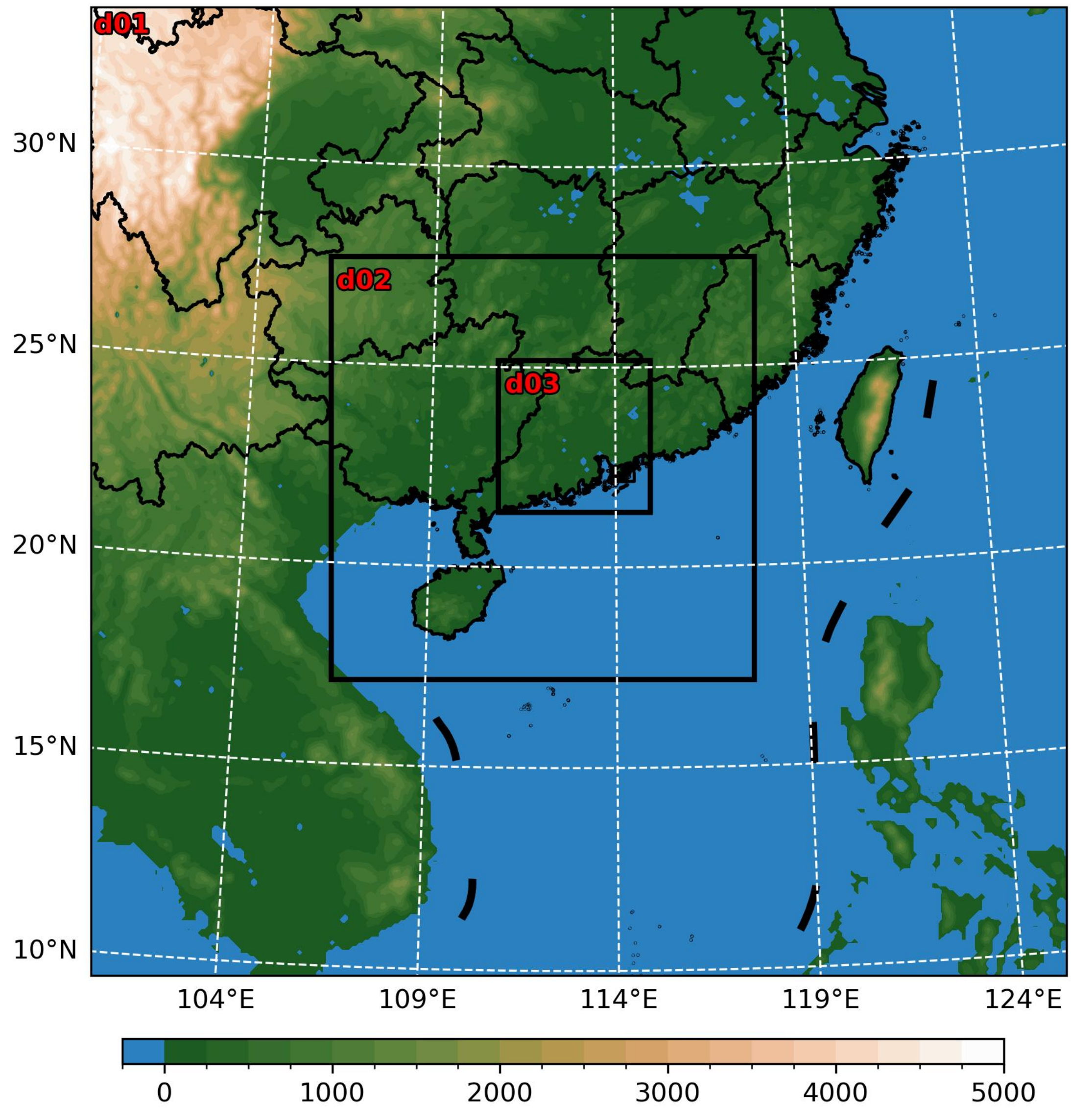

Figure 1: Three two-way nested WRF simulation domains (d01, d02, d03) and terrain-height distribution (unit: m).

Longwave and shortwave radiation are treated with the RRTMG scheme (Iacono et al., 2008), the planetary boundary layer is represented by the Shin–Hong scale-aware scheme (Shin and Hong, 2015), and land-surface processes are represented by the unified Noah model (Tewari et al., 2004). The Tiedtke cumulus parameterization (Zhang et al., 2011) is applied only in the 9 km d01 domain, with no cumulus parameterization in d02 or d03. Cloud microphysics uses the Thompson aerosol-aware scheme (Thompson and Eidhammer, 2014), which includes explicit treatment of aerosol–cloud interactions.

Aerosol initial fields for the Thompson aerosol-aware scheme are derived from the fourth-generation Copernicus Atmosphere Monitoring Service (CAMS) reanalysis dataset, EAC4 (Inness et al., 2019). EAC4 supplies monthly mean aerosol mass-mixing

https://doi.org/10.5194/egusphere-2026-5128
Preprint. Discussion started: 29 September 2026

ratios over 0°–60° N and 50°–150° E for 2003–2022, on a 0.75° × 0.75° grid and 25 pressure levels spanning 1000 to 1 hPa. The aerosol species include size-binned dust, sea salt, hydrophilic/hydrophobic organic carbon and black carbon, and sulfate aerosol. Assuming the lognormal size distribution of Chin et al. (2002), the mass mixing ratios of each component are converted into number concentrations for the Thompson scheme.

The variable lower-boundary condition is imposed only in the lowest model layer. The aerosol surface flux is diagnosed from the near-surface initial concentration and mean surface wind speed using the formulations of Thompson and Eidhammer (2014) and Guo et al. (2024). Using the historical CAMS concentration range, we define five water-friendly aerosol (NWFA) experiments: MIN, 025, AVE, 075, and MAX. The 025 and 075 experiments represent the 25% and 75% positions between MIN and MAX, respectively, while AVE represents the mean level (Fig. 2). All five experiments share identical initial fields, boundary conditions, and physics options and cover the full event life cycle. Aerosol input is the sole perturbed field; therefore, inter-experiment differences isolate relative sensitivity to aerosol perturbations rather than predicting exact real-world concentrations.

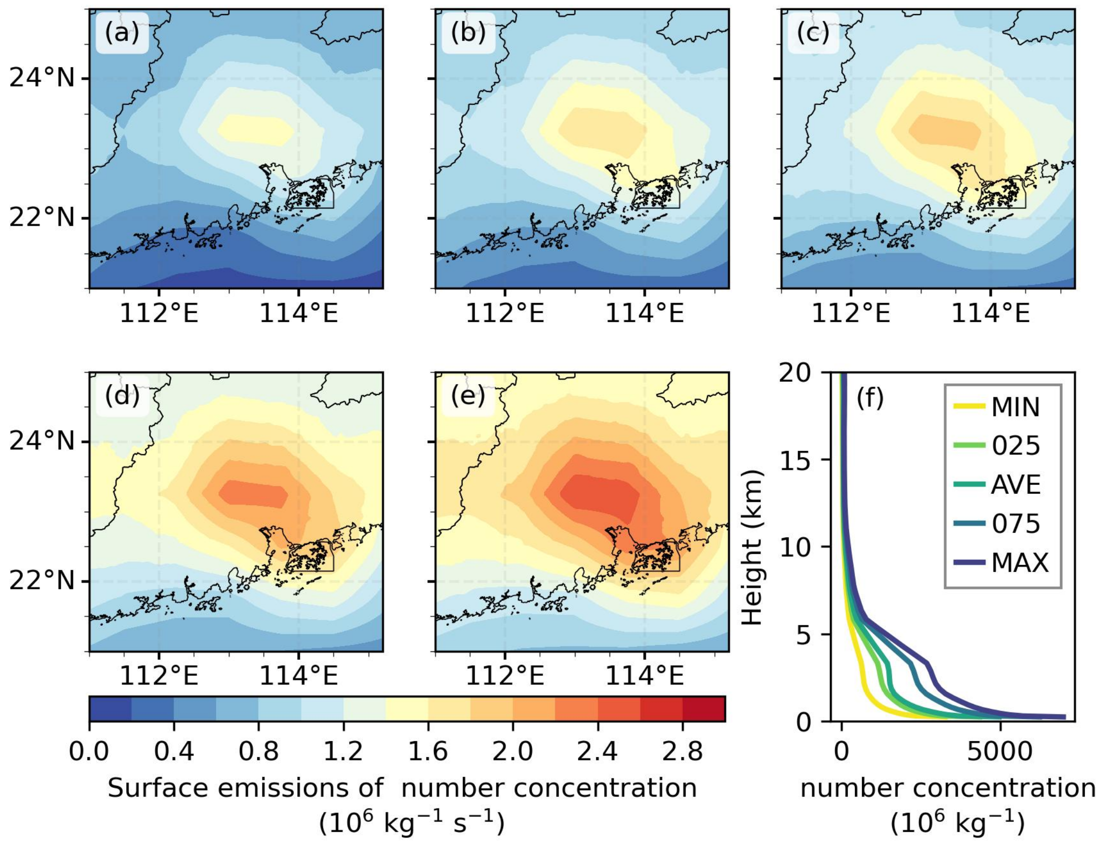

Figure 2: Initial-field distributions of water-friendly aerosol number concentration in the five experiments. (a) MIN, (b) 025, (c) AVE, (d) 075, and (e) MAX show the spatial distributions of surface emission rate (unit: 10^6 kg^{-1} s^{-1}); (f) vertical profiles of water-friendly aerosol number concentration with height in the five experiments (unit: 10^6 kg^{-1}).

https://doi.org/10.5194/egusphere-2026-5128
Preprint. Discussion started: 29 September 2026

2.3 Scale separation based on 2D-DCT

We apply a two-dimensional discrete cosine transform (2D-DCT; Denis et al., 2002) to decompose the spatial scales of the column-integrated total hydrometeor mass field. The input variable $f_{i,j}$ sums the atmospheric-column-integrated masses of cloud droplets, raindrops, ice crystals, snow, and graupel. The 2D-DCT uses even boundary symmetry, which limits high-frequency Gibbs artifacts associated with nonperiodic boundaries in a limited-area domain. The forward transform is:

$$F_{m,n}=\alpha_m\beta_n \sum_{i=0}^{M-1}\sum_{j=0}^{N-1} f_{i,j}\, cos\left[\frac{\pi(2i+1)m}{2M}\right] cos\left[\frac{\pi(2j+1)n}{2N}\right] \tag{1}$$

where $F_{m,n}$ denotes the spectral coefficient, m and n index the x- and y-direction modes, and α_m and β_n denote normalization factors. Let $L_x = M\Delta x$ and $L_y = N\Delta y$; mode (m, n) is assigned the effective horizontal wavelength:

$$\lambda_{m,n}=\frac{2}{\sqrt{(m/L_x)^2+(n/L_y)^2}}, \qquad (m,n)\neq(0,0) \tag{2}$$

The zero mode is treated as the domain-mean background and assigned $\lambda_{0,0} = \infty$. Using the scale-banding framework of Lin and Zhang (2008), we classify wavelengths into the system scale ($\lambda > 150$ km), intermediate scale (50 km $\leq \lambda \leq$ 150 km), and convective scale ($\lambda < 50$ km). The spatial component at scale s is:

$$f_{i,j}^{(s)}=\sum_{m=0}^{M-1}\sum_{n=0}^{N-1} W_{m,n}^{(s)}\, \alpha_m\beta_n F_{m,n} \cos\left[\frac{\pi(2i+1)m}{2M}\right] \cos\left[\frac{\pi(2j+1)n}{2N}\right] \tag{3}$$

where $W_{m,n}^{(s)}$ takes a value of 1 inside the corresponding wavelength range and 0 elsewhere. The original field is recovered by summing the three components, and spectral power is computed from the sum of $F_{m,n}^2$ over the corresponding ranges. These three scales represent the broad hydrometeor background, organization within the rainband, and local intense cores, respectively, and should not be interpreted as unique proxies for specific microphysical or dynamical processes.

2.4 Hydrometeor mass budget

The column hydrometeor mass budget connects surface-precipitation changes with in-cloud microphysical perturbations (Khain, 2009; Cheng et al., 2010; Morrison and Grabowski, 2011). Within the three-dimensional analysis domain, mass conservation for each hydrometeor category is expressed as:

$$\partial X_{col}/\partial t=X_{adv}+X_{top}+X_{bot}+X_{gen}-X_{loss} \tag{4}$$

where X_{col} denotes column-integrated mass of the hydrometeor category (X='C', cloud droplets; X='R', raindrops; X='I', ice crystals; X='S', snow; X='G', graupel). Vertical integration is performed with the midpoint trapezoidal method; X_{adv}, X_{top} and X_{bot} represent transport of hydrometeor mass across the lateral, upper, and lower column boundaries, respectively, while X_{gen} and X_{loss} represent in-column microphysical source and sink terms, respectively.

Because the WRF column has no hydrometeor flux through its upper boundary and raindrop flux through the lower boundary is surface liquid precipitation, Eq. (4) for raindrops becomes

$$P=R_{adv}-\partial R_{col}/\partial t+R_{gen}-R_{loss} \tag{5}$$

https://doi.org/10.5194/egusphere-2026-5128
Preprint. Discussion started: 29 September 2026

where P represents study-region precipitation, R_{loss} is the in-column rainwater sink, dominated by evaporation, R_{gen} is the source term and contains two contributions: (1) rainwater generated by warm-cloud processes (rainwater production rate, R_{warm}), (2) rainwater supplied by ice-phase processes (cold-rain source, R_{cold}). R_{warm} and R_{cold} are diagnosed in Sect. 2.5. Because cloud droplets and ice-phase hydrometeors are fully removed by evaporation or melting before directly reaching the surface, Eq. (4) reduces, for cloud droplets, ice crystals, snow, and graupel, to

$$X_{adv}-\partial X_{col}/\partial t+X_{gen}-X_{loss}=0 \quad (6)$$

2.5 Rainwater source terms

The rainwater production rate term (R_{warm}) contains two contributions: (1) vapor condensation directly onto raindrops (R_{cond}); (2) cloud droplet conversion to rain (R_{cc}). Because R_{cc} also appears in the cloud droplet source–sink budget, Eq. (6) gives

$$R_{cc}=C_{cond}-C_{evap}-C_{rim}+C_{adv}-\partial C_{col}/\partial t \quad (7)$$

where C_{cond} denotes in-column condensational growth of cloud droplets, C_{evap} and C_{rim} denote cloud droplet losses from evaporation and freezing, respectively. The rainwater production rate term (R_{warm}) can then be written as

$$R_{warm}=RC_{cond}-C_{evap}-C_{rim}+C_{adv}-\partial C_{col}/\partial t \quad (8)$$

where RC_{cond} combines condensation onto raindrops and cloud droplets.

The cold-rain source term (R_{cold}) is decomposed into three contributions: (1) net ice-crystal contribution to rainwater (R_{ice}), (2) net snow contribution to rainwater (R_{snow}), (3) net graupel contribution to rainwater (R_{grap}). Using Eq. (4), R_{ice}, R_{snow} and R_{grap} are diagnosed as

$$R_{ice}=I_{rim}+I_{dep}-I_{sub}+I_{adv}-\partial I_{col}/\partial t \quad (9)$$

$$R_{snow}=S_{rim}+S_{dep}-S_{sub}+S_{adv}-\partial S_{col}/\partial t \quad (10)$$

$$R_{grap}=G_{rim}+G_{dep}-G_{sub}+G_{adv}-\partial G_{col}/\partial t \quad (11)$$

where I_{rim}, S_{rim} and G_{rim} denote net in-column riming growth of the ice-phase species, $I_{dep}(I_{sub})$, $S_{dep}(S_{sub})$ and $G_{dep}(G_{sub})$ denote ice-phase mass gain (loss) from deposition (sublimation) within the column.

2.6 Buoyancy equation

Previous studies (Khain et al., 2005; Fan et al., 2009, 2012, 2018) relate precipitation perturbations to changes in convective-scale updraft speed (w). Both parcel-model studies (Rosenfeld et al., 2008) and cloud-resolving-model studies (Fan et al., 2017, 2018) identify buoyancy as a key control on updraft velocity. We compute buoyancy following Fan et al. (2017):

$$B=g\left[\frac{(\theta-\bar{\theta})}{\bar{\theta}}+0.61(q_v-\bar{q}_v)-q_t\right] \quad (12)$$

where θ is potential temperature, an overbar indicates the study-region horizontal mean, g is gravitational acceleration, q_v and q_t are water-vapor and total-hydrometeor mass mixing ratios, respectively. In Eq. (12), the first right-hand-side term is the

https://doi.org/10.5194/egusphere-2026-5128
Preprint. Discussion started: 29 September 2026

temperature-perturbation contribution to buoyancy (hereafter B_{temp}), the second is the water-vapor contribution to buoyancy (hereafter B_{vapr}), and the third is the total-hydrometeor loading term (hereafter B_{hydr}).

2.7 Identification and tracking of intermediate-scale convective elements

Building on TITAN and object-based verification (Dixon and Wiener, 1993; Davis et al., 2006), MCEs are detected and tracked from the 2D-DCT intermediate-scale hydrometeor component. Every 20 min, grid points with original column-integrated total hydrometeor mass $H_{tot} \geq 1$ kg m^{-2} form candidate regions that are labeled with eight-neighbor connectivity. Object area and its intensity-squared-weighted centroid are:

$$A_j = N_j \Delta x \Delta y, \quad r_j = \frac{\sum_{i\in\Omega_j} H_i^2\, r_i}{\sum_{i\in\Omega_j} H_i^2} \tag{13}$$

For each pair of adjacent times, the matching score combines the intensity-squared-weighted intersection-over-union O_{kj}, the linearly extrapolated centroid distance d_{kj}, and the area similarity Q_{kj}:

$$S_{kj} = 0.5 O_{kj} + 0.3\exp\left[-\frac{d_{kj}^2}{2\sigma^2}\right] + 0.2 Q_{kj}, \quad Q_{kj} = \min(A_k, A_j)/\max(A_k, A_j) \tag{14}$$

With σ = 20 km, global maximum-score matching is restricted to object pairs with $d_{kj} \leq 40$ km and $O_{kj} \geq 0.05$. During merging or splitting, the highest-scoring branch is retained as the primary track; unmatched objects start new tracks. Only tracks persisting for at least three consecutive time steps are retained for lifetime and trajectory statistics.

3 Results

3.1 Effects of aerosols on the spatiotemporal distribution of surface precipitation

Observations show a separation between the inland frontal rainband and the coastal warm-sector rainband, with accumulated precipitation exceeding 250 mm around the Pearl River Estuary (Fig. 3). Xiao et al. (2025), using automatic weather stations, dual-polarization radar, and 2DVD observations, showed that a similar model configuration reproduced both rainbands and the overall accumulated-precipitation pattern, although the first coastal rainfall peak occurred 3 h too late. This phase and amplitude bias may reflect a delayed model representation of coastal-convergence triggering and the organization of merged convection into a band. The five experiments use identical initial and boundary conditions and physical configurations, and reasonably reproduce the locations of the two rainbands, accumulated precipitation, and timing of the second peak. Thus, this bias mainly limits the forecast of absolute peak magnitude and does not affect the comparability of responses among the experiments.

https://doi.org/10.5194/egusphere-2026-5128
Preprint. Discussion started: 29 September 2026

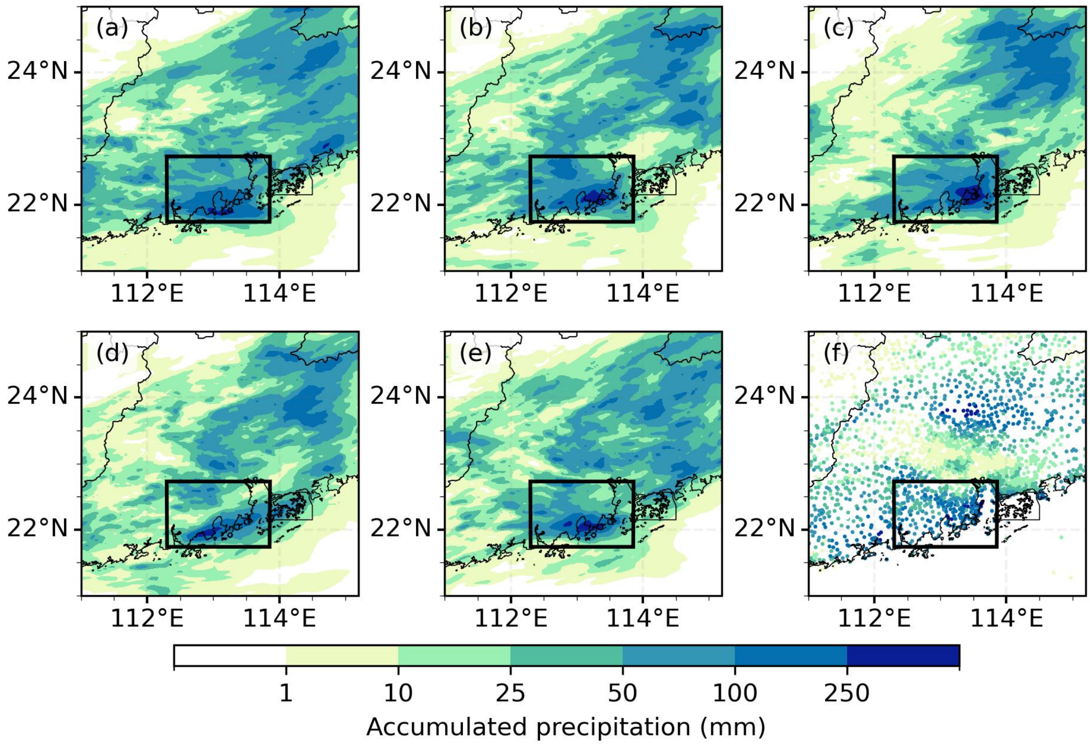

Figure 3: Spatial distribution of 24-h accumulated precipitation from 12:00 UTC 10 May to 12:00 UTC 11 May 2022 in the five simulations and observations (unit: mm). Panels (a)–(f) correspond to MIN, 025, AVE, 075, MAX, and observations, respectively.

All five experiments retain the inland frontal rainband and the coastal warm-sector rainband; their differences are mainly reflected in the organization of heavy coastal precipitation (Fig. 3). In MIN and 025, the heavy-rain centers are relatively scattered and areas exceeding 250 mm lack continuity. When the aerosol concentration increases to AVE, a more concentrated and continuous heavy-rain belt forms west of the Pearl River Estuary and along the coast, most closely matching the observed location of extreme precipitation. With further increases to 075 and MAX, the rainband gradually narrows, breaks apart, and becomes discrete clusters. Although MAX recovers some local heavy precipitation, its continuity remains weaker than in AVE. Along the concentration gradient, coastal heavy precipitation evolves from a dispersed pattern at low concentrations toward a more concentrated and continuous pattern, reaches its most coherent organization near the moderate concentration, and then fragments again as concentration increases further. Aerosol perturbations therefore mainly alter the concentration and continuity of the coastal MCS rainband rather than substantially shifting the basic positions of the two rainbands.

https://doi.org/10.5194/egusphere-2026-5128
Preprint. Discussion started: 29 September 2026

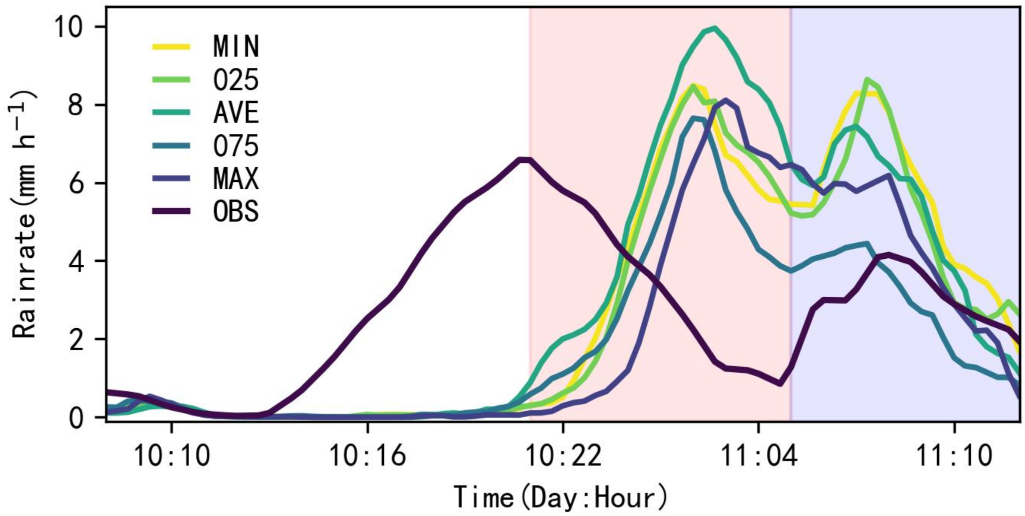

Figure 4: Time evolution of the study-area-mean rainfall rate (unit: mm h^{-1}). Shading marks the two diagnostic stages of interest: the primary-rainband development stage (21:00 UTC to 05:00 UTC), corresponding to rapid development and the first peak; and the later organizational adjustment stage (05:00 UTC to 12:00 UTC), corresponding to the second peak, plateau maintenance, or local recovery.

Figure 4 shows a clear stage dependence of the rainfall-rate response to aerosol concentration. The full-period peaks in MIN and 025 are 8.478 and 8.628 mm h^{-1}, respectively, while AVE reaches 9.945 mm h^{-1}. During the development stage, the mean rainfall intensity increases from 4.623 mm h^{-1} in MIN to 5.907 mm h^{-1} in AVE, then decreases to 3.852 and 3.678 mm h^{-1} in 075 and MAX, respectively. During the adjustment stage, MAX recovers to 4.326 mm h^{-1}, but remains below 5.517, 5.061, and 4.929 mm h^{-1} in MIN, 025, and AVE, respectively. Along the concentration gradient, precipitation first increases and then decreases during the primary intensification stage; the late recovery at the highest concentration is mainly local and does not alter the overall decrease in system-mean rainfall intensity.

3.2 Multiscale characteristics of hydrometeors and their responses to aerosol concentration

When precipitation transitions from a continuous rainband to discrete clusters, changes occur not only in total hydrometeor amount but also in its allocation across spatial scales. The DCT components are used to distinguish these two types of change. The system scale represents the overall background constrained by circulation and moisture transport; the intermediate scale retains continuous rainband segments, cell arrangement, and cluster boundaries; and the convective scale highlights local intense cores and newly initiated cells. Together, the three components reconstruct the full hydrometeor field, allowing us to test whether aerosols primarily modify the event-scale background or the internal organization of the MCS.

https://doi.org/10.5194/egusphere-2026-5128
Preprint. Discussion started: 29 September 2026

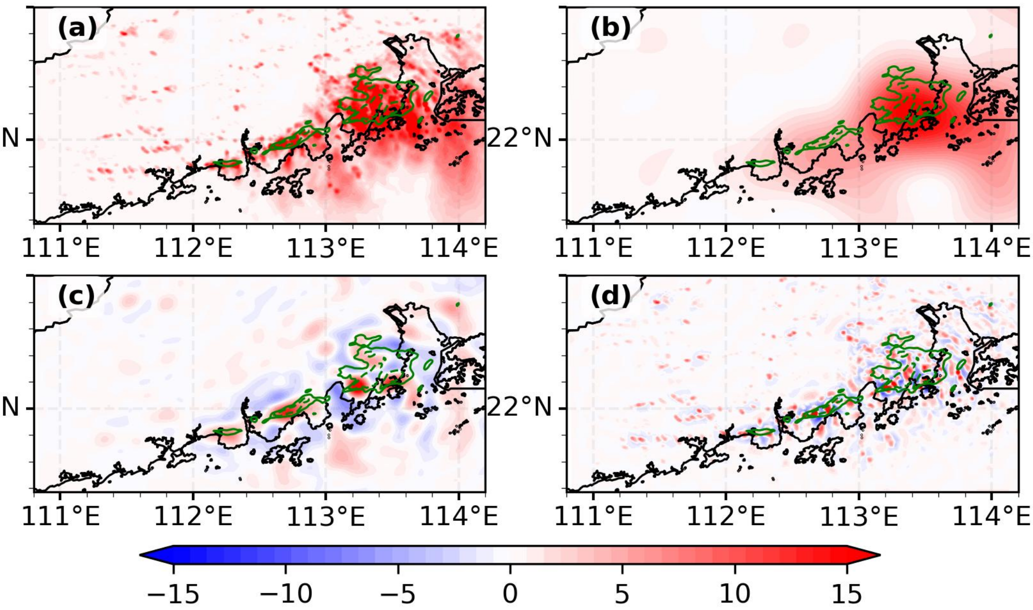

Figure 5: Column-integrated total hydrometeor mass field (unit: kg m^{-2}) and scale-separation results for the AVE experiment at 02:00 UTC 11 May 2022. (a) Original field; (b) system scale (>150 km); (c) intermediate scale (50–150 km); (d) convective scale (<50 km). The green solid contour denotes 10 mm 20 min^{-1} precipitation and the green dashed contour denotes 20 mm 20 min^{-1} precipitation.

Figure 5 provides an example of the scale decomposition for the AVE experiment at 02:00 UTC 11 May. The original column-integrated total hydrometeor field contains both the coastal rainband and local intense cores; the system-scale component retains the continuous background, the intermediate-scale component highlights continuous segments and cluster boundaries within the rainband, and the convective-scale component retains local intense cores. Figure 6 further compares the temporal evolution of spectral power at the three scales.

https://doi.org/10.5194/egusphere-2026-5128
Preprint. Discussion started: 29 September 2026

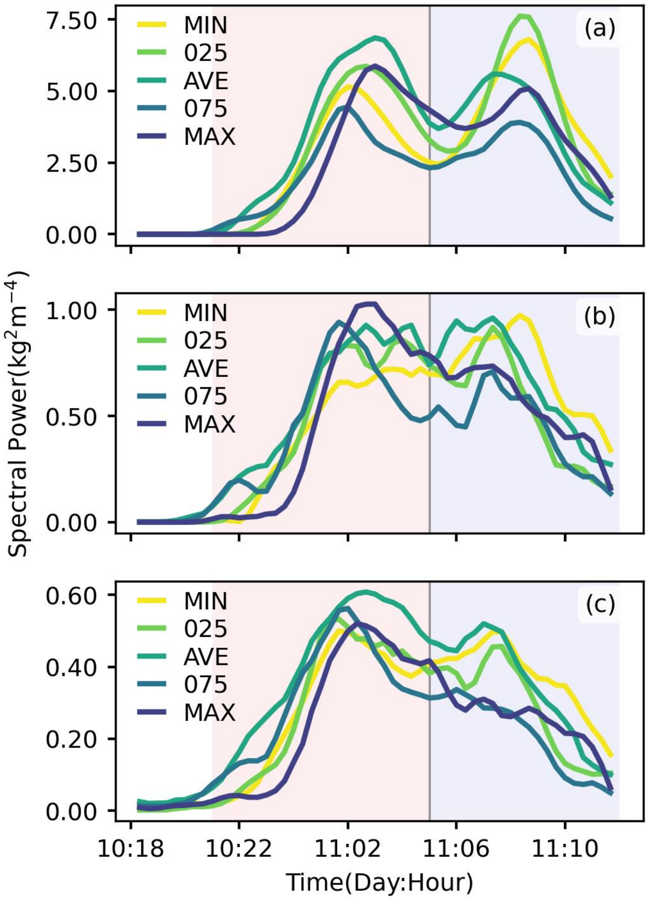

Figure 6: Time evolution of spectral power at each scale in the hydrometeor-integrated field under different aerosol backgrounds (unit: kg^2 m^{-4}). (a) System-scale component (λ > 150 km); (b) intermediate-scale component (50 km $\leq \lambda \leq$ 150 km); (c) convective-scale component (λ < 50 km). Shading indicates the two diagnostic stages: the development stage, corresponding to rapid development and the first peak; and the adjustment stage, corresponding to the second peak, plateau maintenance, or local recovery.

System-scale spectral power shows a similar double-peaked evolution in all five experiments: the first peak occurs at 02:00–03:00 UTC on 11 May, followed by a decline and then renewed enhancement at 07:00–09:00 UTC (Fig. 6a). The first peak is highest in AVE at 6.970 kg^2 m^{-4}; MAX and 025 reach 5.991 and 5.916 kg^2 m^{-4}, while MIN and 075 reach 5.276 and 4.592 kg^2 m^{-4}. The ranking changes for the second peak, with 025 and MIN increasing to 7.774 and 6.945 kg^2 m^{-4}, higher than the 5.687, 5.205, and 3.945 kg^2 m^{-4} in AVE, MAX, and 075. The common double-peaked pattern indicates that aerosol perturbations modify the amplitude and timing of system-scale hydrometeor variability more strongly than the underlying large-scale rainband structure.

Differences in intermediate-scale spectral power among the experiments are expressed mainly in peak timing and the duration of high values (Fig. 6b). Peak values in the five experiments fall within 0.934–1.098 kg^2 m^{-4}. The maxima in MIN and 025 are delayed to 08:20 and 07:00 UTC, respectively; AVE approaches 1.0 kg^2 m^{-4} several times around 04:00, 06:00, and 07:20 UTC, with high values persisting into the maintenance stage; 075 and MAX reach 0.998 and 1.098 kg^2 m^{-4} relatively early and

https://doi.org/10.5194/egusphere-2026-5128
Preprint. Discussion started: 29 September 2026

then decline markedly. Along the concentration gradient, intermediate-scale activity shifts from late-stage peaks in MIN and 025, to sustained high values in AVE, and then to early peaks followed by rapid decline in 075 and MAX. Importantly, similar spectral power does not imply the same organizational form: both a continuous rainband and multiple discrete clusters can generate high power, and these configurations are distinguished further in the next section.

Differences among the experiments are more concentrated at the convective scale (Fig. 6c). Peak values for MIN, 025, AVE, 075, and MAX are 0.527, 0.570, 0.627, 0.569, and 0.527 kg^2 m^{-4}, respectively, with AVE reaching the highest value around 03:00 UTC. After 06:00 UTC, AVE also exhibits a secondary maximum of 0.532 kg^2 m^{-4}, while MIN and 025 recover to 0.518 and 0.514 kg^2 m^{-4} over the same period; the late-stage highs in 075 and MAX are only 0.343 and 0.345 kg^2 m^{-4}. From MIN to AVE, convective-scale spectral power progressively increases and retains a pronounced secondary maximum after 06:00 UTC; with further increases to 075 and MAX, the peak declines and the late-stage high is also markedly weaker.

Across all three scales, the five experiments retain a similar double-peaked framework at the system scale, indicating that the system-scale hydrometeor background of the event is relatively stable. As aerosol concentration increases from MIN to AVE, convective-scale spectral power progressively strengthens and high intermediate-scale values persist into the maintenance stage; when concentration increases further to 075 and MAX, the convective-scale peak declines and high intermediate-scale values also decay earlier. Aerosols therefore primarily regulate the allocation of hydrometeor signals among spatial scales and life cycle stages, with the response turning near the moderate concentration.

3.3 Response of intermediate-scale convective organization to aerosols

To reduce short-term fluctuations in MCE number and emphasize organizational evolution, we divide the event into five periods for the statistics in this section: initiation (19:00–22:00 UTC), development (22:00–01:00 UTC), peak (01:00–04:00 UTC), maintenance (04:00–08:00 UTC), and decay (08:00–12:00 UTC). For each period, MCE numbers are compared in the order MIN, 025, AVE, 075, and MAX, and their spatial evolution is analyzed together with the centroid tracks in Fig. S2 and composite reflectivity in Figs. S3–S7. The MCE identification and tracking method is described in Sect. 2.7.

https://doi.org/10.5194/egusphere-2026-5128
Preprint. Discussion started: 29 September 2026

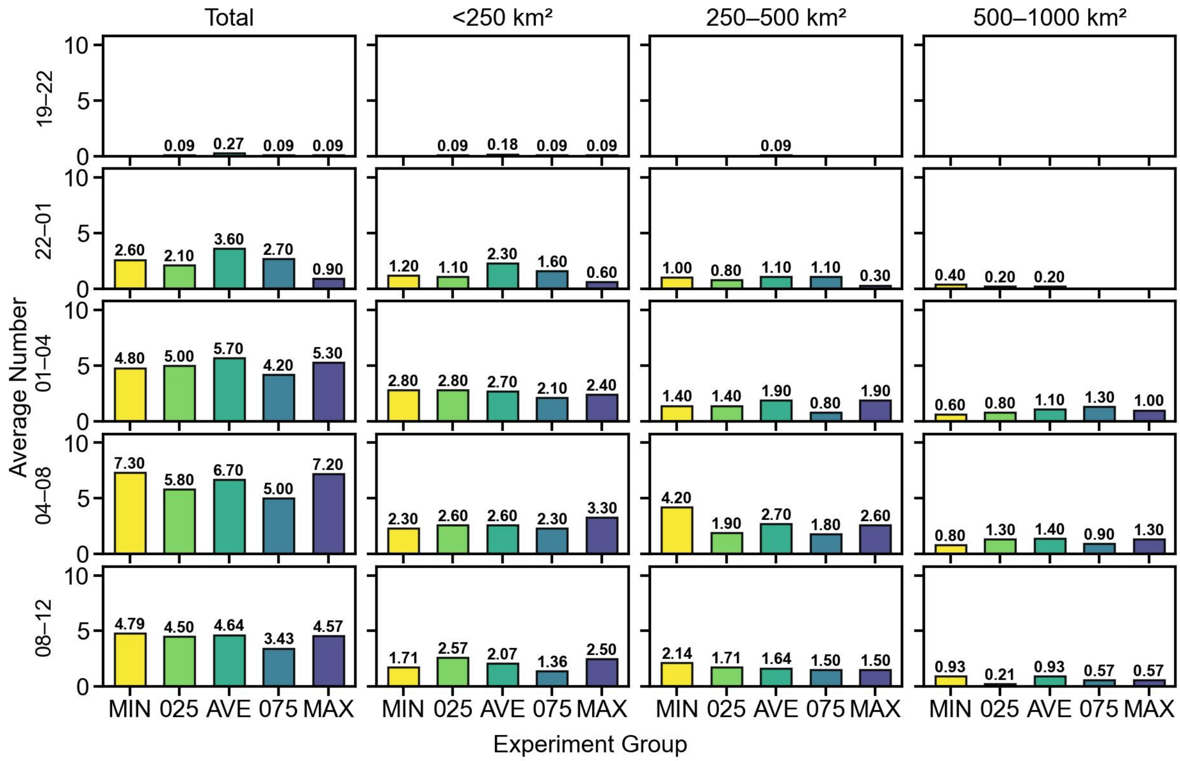

Figure 7: Mean numbers of intermediate-scale convective elements (MCEs) for different area thresholds during different precipitation-characteristic periods under different aerosol backgrounds. Each row corresponds to one period, from top to bottom: initiation (19:00–22:00 UTC), development (22:00–01:00 UTC), peak (01:00–04:00 UTC), maintenance (04:00–08:00 UTC), and decay (08:00–12:00 UTC). Columns correspond to total, <250 km² (small), 250–500 km² (medium), and 500–1000 km² (large), respectively. Each panel compares the five experiments MIN, 025, AVE, 075, and MAX.

Figure 7 together with Fig. S2 and Figs. S3–S7 shows that aerosol concentration simultaneously adjusts the timing of MCE formation, area composition, and along-coast organization. No MCE is identified during the initiation stage in MIN. During the rapid-intensification stage, the mean total number is 2.60, comprising 1.20 small, 1.00 medium, and 0.40 large elements. The total increases to 4.80 during the peak stage and further to 7.30 during maintenance, mainly because medium elements increase to 4.20; 4.79 elements remain during decay, including 2.14 medium and 0.93 large elements. Figs. S2 and S3 show that MCE tracks in MIN are scattered and strong echoes evolve into multiple parallel cores, so the increase in element number does not form a stable, concentrated band of strong echoes along the coast.

When the aerosol concentration increases to 025, MCEs begin to appear during initiation, but the mean totals during rapid intensification and maintenance are 2.10 and 5.80, both lower than in MIN. The total reaches 5.00 during the peak stage, with 2.80 small, 1.40 medium, and 0.80 large elements; during decay, small elements increase to 2.57 while large elements decrease to 0.21. The tracks and composite reflectivity likewise show multiple relatively independent movement paths and strong-echo centers, indicating that 025 mainly changes the area composition of the elements without substantially increasing the spatial connectivity of coastal convection.

https://doi.org/10.5194/egusphere-2026-5128
Preprint. Discussion started: 29 September 2026

MCE activity appears earlier in AVE. During initiation, the mean total is 0.27, including 0.18 small elements, and AVE is the only experiment with a medium element at this stage. During rapid intensification, the total increases to the highest among the five experiments, 3.60, mainly comprising 2.30 small and 1.10 medium elements; during the peak stage, the total further increases to 5.70, with 1.90 medium and 1.10 large elements. The total increases further to 6.70 during the maintenance stage, while the mean numbers of medium and large elements remain at 2.70 and 1.40, respectively. Consistent with the number and area composition, the principal tracks in Fig. S2 extend continuously along the coast, and the strong-echo cores from the peak to maintenance stages in Fig. S5 connect into a relatively complete northeast–southwest-oriented echo band. Thus, from low aerosol concentrations to AVE, not only are more MCEs generated during rapid intensification, but medium and large elements also continue to develop in subsequent stages, organizing coastal convection from dispersed cores into a continuous rainband. With a further increase to 075, the mean total during rapid intensification decreases from 3.60 in AVE to 2.70, and then to 4.20, 5.00, and 3.43 during the peak, maintenance, and decay stages, respectively. Although large elements reach 1.30 during the peak stage—the highest concurrent value among the five experiments—medium elements number only 0.80, indicating that enlargement of individual elements does not translate into stronger overall MCE activity; the strong-echo band and movement tracks in Fig. S6 also become interrupted relatively early. The evolution in MAX is shifted markedly later: the mean total during rapid intensification is only 0.90, with no large elements; the total recovers to 5.30 during the peak stage and rises further to 7.20 during maintenance, when small elements reach the highest value among the five experiments, 3.30, and medium and large elements reach 2.60 and 1.30. Figs. S2 and S7 show that multiple strong-echo cores reappear late in MAX, but these cores and their movement paths remain relatively dispersed.

Across the five experiments, MCE organization shows a clear two-stage change with aerosol concentration. From MIN through 025 to AVE, MCEs appear earlier, more elements form during rapid intensification, medium and large elements continue to develop through the peak and maintenance stages, and along-coast tracks and strong echoes progressively connect into a continuous rainband. With further increases to 075 and MAX, MCE activity either weakens earlier or increases again later; however, the late increase in MAX consists mainly of multiple discrete cores and does not recover the continuous along-coast organization seen in AVE. Thus, a larger number of elements does not necessarily imply greater rainband continuity. The key is whether elements at different scales can form a sustained regeneration chain.

These results show that MCE number and area composition alone are insufficient to explain changes in rainband continuity. We next compare system-scale and convective-scale rainwater budgets to determine whether regionally averaged rainwater generation increases as aerosol concentration rises, and whether local recovery at high concentration relies mainly on hydrometeor transport and cold-rain compensation, thereby distinguishing continuous regeneration from local compensation.

3.4 Response of the system-scale rainwater budget to aerosols

Based on the 2D-DCT definition of system-scale wavelengths greater than 150 km, we select a 200 km × 170 km region covering the primary precipitation area of the coastal South China MCS (Fig. 3). The region spans the system scale in both horizontal directions and fully contains the primary coastal rainband, so its area-mean mass budget can represent system-scale

https://doi.org/10.5194/egusphere-2026-5128
Preprint. Discussion started: 29 September 2026

rainwater generation, loss, and transport within the MCS. We further compare the two stages shown in Fig. 4: the development stage, covering rapid precipitation intensification and the first peak, and the adjustment stage, covering the second peak, plateau maintenance, or local recovery, to analyze stage-dependent changes in the system-scale rainwater budget with aerosol concentration.

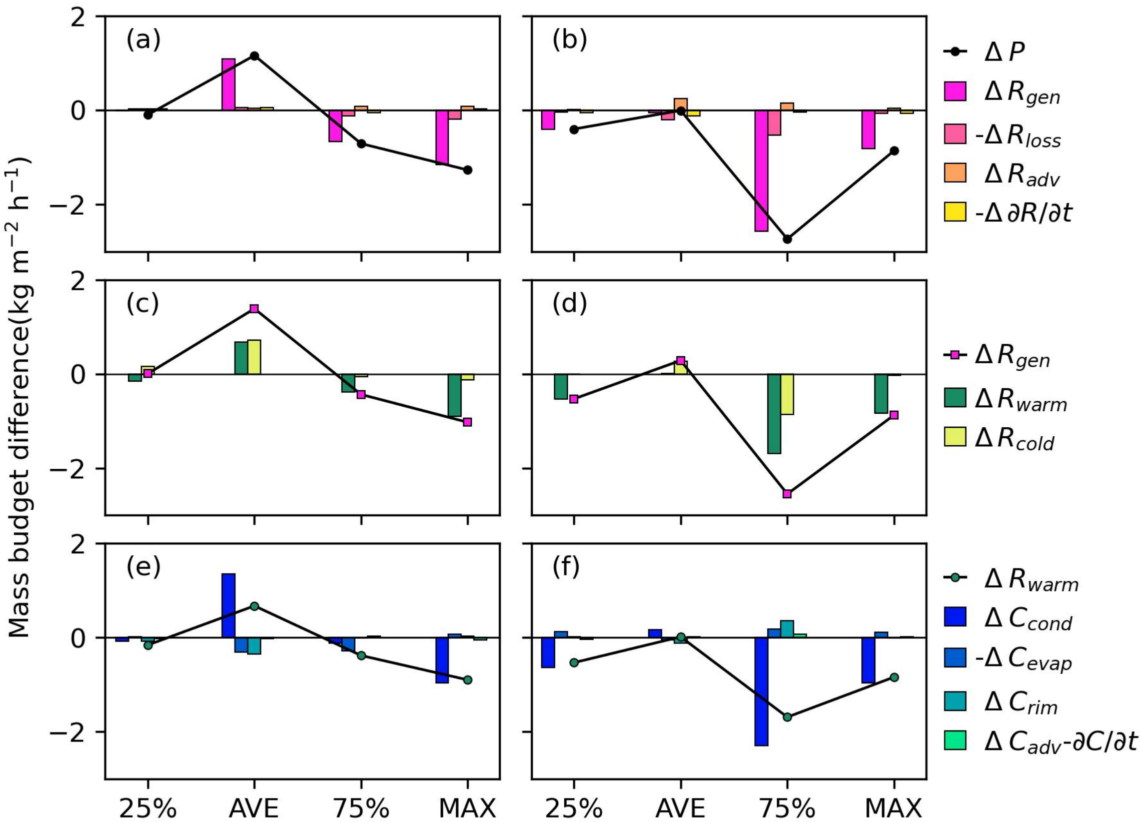

Figure 8: Aerosol impacts on the time-averaged study-area-mean rainwater mass budget, expressed as differences relative to the MIN experiment. (a, b) Differences in surface precipitation (ΔP) and the break-down terms of the rainwater mass-budget equation (Eq. (5)), including rainwater generation (ΔRgen), rainwater loss (−ΔRloss), lateral advection (ΔRadv), and storage change (−Δ∂R/∂t); (c, d) differences in rainwater generation (ΔRgen) decomposed into warm-rain (ΔRwarm) and cold-rain (ΔRcold) contributions; (e, f) differences in warm-rain generation (ΔRwarm) and the break-down terms of the warm-rain budget (Eq. (8)), including condensation, cloud droplet evaporation, the cloud droplet riming/freezing sink, and cloud-water advection/storage. Panels in the left column are averaged over the primary-rainband development stage (21:00 UTC 10 May–05:00 UTC 11 May), and panels in the right column over the later organizational adjustment stage (05:00–12:00 UTC 11 May). Unit: kg m^{-2} h^{-1}.

System-scale differences in surface precipitation are controlled primarily by the rainwater-generation term and vary non-monotonically with aerosol concentration (Fig. 8a, b). During the development stage, ΔRgen in 025 is close to neutral (−0.03 kg m^{-2} h^{-1} relative to MIN), whereas AVE increases by 1.15 kg m^{-2} h^{-1}. The associated rainwater-loss, advection, and storage-change terms remain small, with magnitudes of 0.06, 0.04, and 0.05 kg m^{-2} h^{-1}, respectively. In 075 and MAX, ΔRgen turns negative, decreasing by 0.66 and 1.20 kg m^{-2} h^{-1}, while the negative contribution from rainwater loss increases to 0.12 and 0.19 kg m^{-2} h^{-1}. The precipitation increase in AVE during the primary intensification stage therefore arises mainly from local

https://doi.org/10.5194/egusphere-2026-5128
Preprint. Discussion started: 29 September 2026

raindrop generation; the high-concentration experiments first exhibit insufficient generation, accompanied by stronger evaporative loss.

During the adjustment stage, the high-concentration response no longer decreases continuously. ΔRgen in 025 and AVE remains close to MIN, at −0.43 and −0.03 kg m^{-2} h^{-1}, respectively; 075 decreases to −2.65 kg m^{-2} h^{-1}, whereas MAX is −0.85 kg m^{-2} h^{-1}. Over the same period, ΔRadv in 025, AVE, 075, and MAX is 0.02, 0.24, 0.15, and 0.04 kg m^{-2} h^{-1}, respectively. Compared with the development stage, the negative rainwater-generation anomaly in MAX narrows from −1.20 to −0.85 kg m^{-2} h^{-1}, indicating improved regionally averaged rainwater generation, although it remains lower than in MIN.

Source-term decomposition shows that AVE enhances both warm- and cold-rain processes during the development stage (Fig. 8c–f). Its ΔRwarm and ΔRcold increase by 0.58 and 0.57 kg m^{-2} h^{-1}, respectively, giving a combined enhancement consistent with the approximately 1.15 kg m^{-2} h^{-1} increase in ΔRgen. In 025 the two contributions approximately cancel. In 075 and MAX, ΔRwarm decreases by 0.40 and 0.82 kg m^{-2} h^{-1}, while ΔRcold is −0.26 and −0.38 kg m^{-2} h^{-1}, respectively, so cold-rain processes do not make up the deficit. In the warm-rain decomposition, the condensational-growth term ΔRCcond increases by 1.35 kg m^{-2} h^{-1} in AVE but decreases by 0.96 kg m^{-2} h^{-1} in MAX. During the adjustment stage, ΔRwarm in 075 and MAX remains lower by 1.60 and 0.78 kg m^{-2} h^{-1}, while the corresponding cold-rain anomalies are −1.05 and −0.07 kg m^{-2} h^{-1}. These results indicate that the precipitation increase from MIN to AVE is initiated by stronger condensational growth and warm-rain production and subsequently amplified by ice-phase conversion. At higher aerosol loadings, the main deficit arises from the loss of a sustained rainwater production rate.

Changes in the cloud droplet spectrum provide direct evidence for the warm-rain transition (Fig. S8). From MIN to MAX, during the development stage the mean cloud droplet diameter in the condensation region ($S > 0$) decreases from 19.100 to 14.064 μm, while number concentration increases from 1.234×10^8 to 3.372×10^8 m^{-3}; in the evaporation region ($S < 0$), mean diameter decreases from 30.431 to 20.401 μm, while number concentration increases from 1.472×10^8 to 6.206×10^8 m^{-3}. From MIN to AVE, the increase in activated droplets can still support condensational growth and the collection of cloud water by raindrops. With further increases in concentration, the mean droplet size decreases, collision–coalescence efficiency declines, and evaporative cooling and rainwater loss strengthen. The simultaneous changes in droplet size and number concentration are consistent with the turning points in condensational growth, cloud-water collection by raindrops, and rainwater loss in Fig. 8, indicating that warm-rain formation efficiency in this set of simulations is highest near AVE and decreases in 075 and MAX.

https://doi.org/10.5194/egusphere-2026-5128
Preprint. Discussion started: 29 September 2026

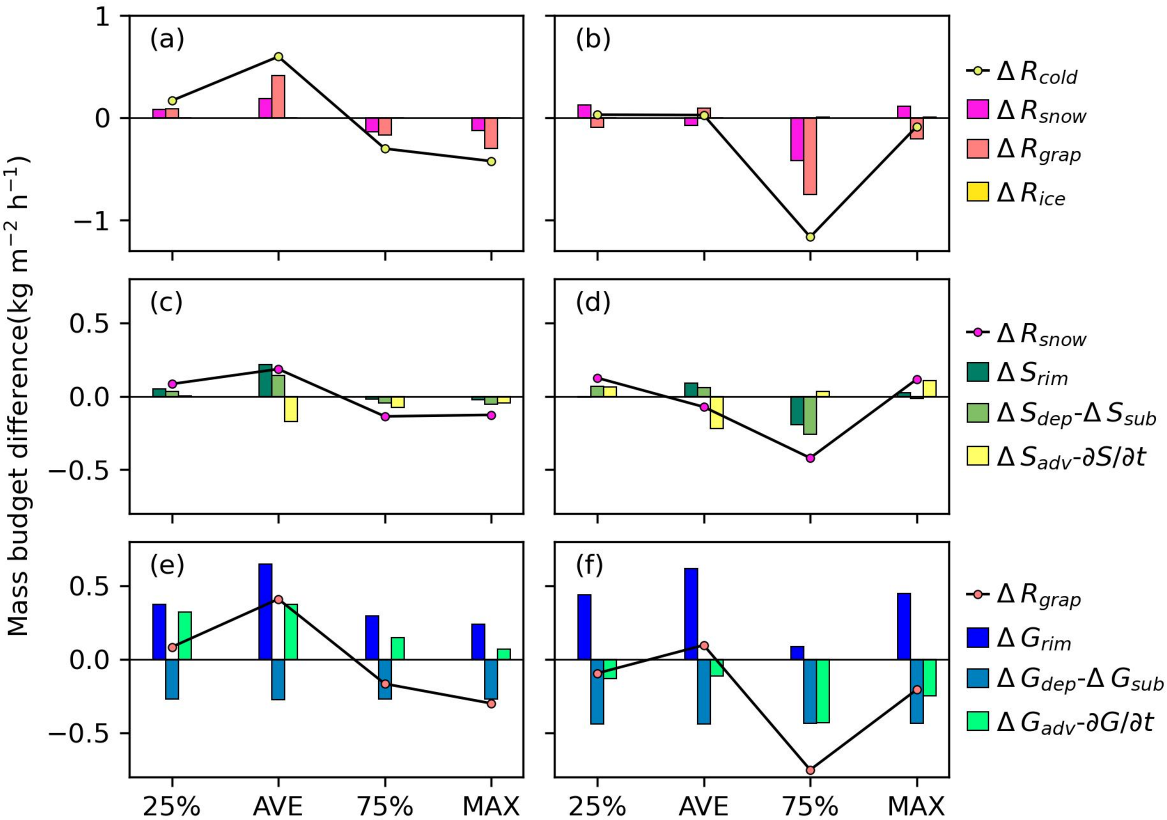

Figure 9: Aerosol impacts on the time-averaged study-area-mean cold-rain source budget, expressed as differences relative to the MIN experiment. (a, b) Differences in the total cold-rain source (ΔRcold) and its contributions from net conversion of ice crystals (ΔRice), snow (ΔRsnow), and graupel (ΔRgrap) to raindrops; (c, d) differences in the snow contribution (ΔRsnow) and the breakdown terms of the snow mass-budget diagnostic (Eq. (10)), including riming (ΔSrim), net deposition minus sublimation (ΔSdep − ΔSsub), and lateral-advection/storage change (ΔSadv − Δ∂S/∂t); (e, f) differences in the graupel contribution (ΔRgrap) and the breakdown terms of the graupel mass-budget diagnostic (Eq. (11)), including riming (ΔGrim), net deposition minus sublimation (ΔGdep − ΔGsub), and lateral-advection/storage change (ΔGadv − Δ∂G/∂t). Panels in the left column are averaged over the primary-rainband development stage (21:00 UTC 10 May–05:00 UTC 11 May), and panels in the right column over the later organizational adjustment stage (05:00–12:00 UTC 11 May). Unit: kg m^{-2} h^{-1}.

Cold-rain processes amplify precipitation in AVE during the primary intensification stage but do not provide equally stable compensation in the high-concentration experiments (Fig. 9). During development, the combined snow, graupel, and ice-crystal contribution in AVE increases by 0.57 kg m^{-2} h^{-1} relative to MIN; 025 shows only a weak positive anomaly, while 075 and MAX decrease by 0.26 and 0.38 kg m^{-2} h^{-1}, respectively. During the adjustment stage, the summed cold-rain components in 025 and AVE are close to neutral, 075 decreases by 1.05 kg m^{-2} h^{-1}, and the decrease in MAX narrows to 0.07 kg m^{-2} h^{-1}. As aerosol loading increases further, signs of late-stage cold-rain compensation emerge.

Fig. S9 traces the source-term changes to specific microphysical processes. In both stages, the summed differences in ice-crystal-related processes are −0.02 to 0.004 kg m^{-2} h^{-1}, clearly smaller than those of the warm-rain, snow, and graupel processes. System-scale precipitation differences therefore arise mainly from the combination of cloud-water condensation, collection of

https://doi.org/10.5194/egusphere-2026-5128
Preprint. Discussion started: 29 September 2026

cloud water by raindrops, and snow/graupel riming and melting. Not all processes vary in the same direction; rather, enhancement or mismatch among a few controlling processes determines the net response.

In 025 during the development stage, warm-rain processes decrease slightly and are compensated by snow processes. The warm-rain contribution decreases by 0.333 kg m^{-2} h^{-1}, snow processes increase by 0.401 kg m^{-2} h^{-1}, and graupel processes increase by only 0.023 kg m^{-2} h^{-1}. The change from MIN to 025 alleviates CCN limitation but does not yet establish a stable warm-rain advantage. AVE, in contrast, enhances warm-rain, snow, and graupel processes simultaneously by 3.257, 0.857, and 0.327 kg m^{-2} h^{-1}, respectively. The positive warm-rain anomaly comes mainly from the positive branch of cloud-water condensation, VCD+ (+2.069 kg m^{-2} h^{-1}), and collection of cloud water by raindrops, RCW (+0.778 kg m^{-2} h^{-1}), which together account for 87% of the positive warm-rain anomaly; cloud-water autoconversion, WAU, instead decreases slightly by 0.125 kg m^{-2} h^{-1}. Thus, the warm-rain enhancement in AVE depends on the combined effects of condensational growth and cloud-water collection by raindrops rather than on a general strengthening of autoconversion.

Snow and graupel processes in AVE are linked to the warm-rain pathway. The positive branch of snow deposition (SDE+), collection of supercooled cloud water by snow (SCW-S), and snow melting (SML) increase by 0.303, 0.250, and 0.195 kg m^{-2} h^{-1}, respectively; collection of supercooled cloud water by graupel (SCW-G) and graupel melting (GML) increase by 0.204 and 0.208 kg m^{-2} h^{-1}. These increases show that, in addition to low-level condensation and raindrop growth, the supply of supercooled cloud water near the 0 °C level, riming growth, and melting also contribute to precipitation enhancement. The collection of graupel by raindrops (RCG), however, decreases by 0.242 kg m^{-2} h^{-1}, so AVE cannot be characterized simply as a general strengthening of ice-phase processes. A more accurate interpretation is that the warm-rain pathway provides a stable water source, while snow/graupel riming and melting increase precipitation production during the primary intensification stage.

When concentration increases to 075 and MAX, the warm-rain pathway weakens first (Fig. S9). During development, the warm-rain processes in the two experiments decrease by 0.815 and 1.866 kg m^{-2} h^{-1}, respectively, mainly because VCD+, RCW, and WAU all decline: the three terms are −0.405, −0.329, and −0.313 kg m^{-2} h^{-1} in 075, and −0.925, −0.414, and −0.342 kg m^{-2} h^{-1} in MAX. Although snow processes in MAX increase slightly by 0.093 kg m^{-2} h^{-1}, graupel processes decrease by 0.219 kg m^{-2} h^{-1} and cannot offset the warm-rain loss. Ice-phase processes remain active under high aerosol loading. The precipitation reduction begins when condensational growth and collection of cloud water by raindrops lose their stable supply, and subsequent ice-phase growth and melting cannot fill the deficit.

During the adjustment stage, warm-rain processes in 025, AVE, 075, and MAX are all lower than in MIN by −1.210, −1.130, −5.715, and −3.238 kg m^{-2} h^{-1}, respectively. The negative anomalies in 075 and MAX are still controlled mainly by VCD+ and RCW: in 075 the two terms decrease by 3.227 and 1.387 kg m^{-2} h^{-1}, and in MAX by 1.856 and 0.838 kg m^{-2} h^{-1}. Snow processes decrease by 0.509 and 1.037 kg m^{-2} h^{-1} in AVE and 075; the net graupel contribution is negative in every non-MIN experiment, with decreases of 0.462 and 0.227 kg m^{-2} h^{-1} in 075 and MAX. Although 075 and MAX show positive RCG anomalies of 0.432 and 0.206 kg m^{-2} h^{-1}, respectively, the net contributions of snow and graupel processes remain negative, indicating that enhancement of a single ice-phase conversion process has not translated into an increase in the regionally averaged cold-rain source.

https://doi.org/10.5194/egusphere-2026-5128
Preprint. Discussion started: 29 September 2026

Figures 8–9 and Fig. S9 collectively show that the system-scale rainwater budget first strengthens and then weakens as aerosol concentration increases. From low to moderate aerosol levels, condensational growth and cloud-water collection by raindrops intensify first, establishing a relatively stable warm-rain water source; the increased supercooled cloud water further promotes snow and graupel riming growth and melting, simultaneously strengthening cold-rain processes. With further aerosol increases, mean cloud droplet size decreases, condensational growth and cloud-water collection by raindrops weaken, and system-mean rainwater generation declines. Although several ice-phase processes recover somewhat later, they offset only part of the warm-rain loss and do not reverse the overall weakening of system-scale precipitation.

3.5 Response of the convective-scale rainwater budget to aerosols

Regional averaging smooths local variations in convective intense cores. To characterize the convective-scale response, Fig. S10 selects, for each experiment and each of the two stages, a 10 km × 10 km area with the highest convective-scale PSD as a representative intense core, and then analyzes its internal rainwater budget and cold-rain processes. During development, high-PSD regions in MIN and 025 are scattered along the coast, AVE forms a relatively continuous high-PSD belt near the 100-mm accumulated-precipitation contour, and the high values in 075 and MAX are more fragmented. During the adjustment stage, the high-PSD core in AVE remains within the continuous precipitation band, whereas MAX exhibits discrete local maxima. Figures 10–11 therefore focus on why enhanced local processes at higher aerosol concentrations still fail to maintain system-scale precipitation.

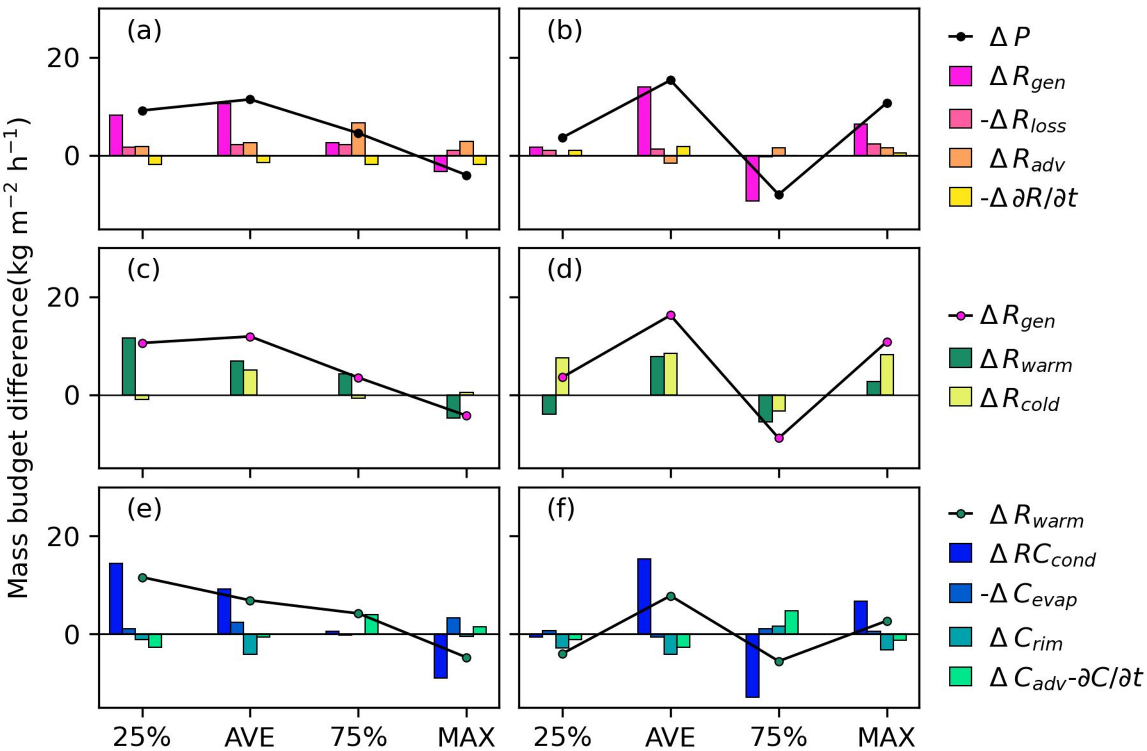

https://doi.org/10.5194/egusphere-2026-5128
Preprint. Discussion started: 29 September 2026

Figure 10: Aerosol impacts on the time-averaged rainwater mass budget within representative convective-scale cores, expressed as differences relative to the corresponding MIN core. For each experiment and stage, the representative core is the 10 km × 10 km box with the maximum convective-scale power spectral density (PSD) shown in Fig. S10. (a, b) Differences in surface precipitation (ΔP) and the break-down terms of the rainwater mass-budget equation (Eq. (5)), including rainwater generation (ΔRgen), rainwater loss (−ΔRloss), lateral advection (ΔRadv), and storage change (−Δ∂R/∂t); (c, d) differences in rainwater generation (ΔRgen) decomposed into warm-rain (ΔRwarm) and cold-rain (ΔRcold) contributions; (e, f) differences in warm-rain generation (ΔRwarm) and the break-down terms of the warm-rain budget (Eq. (8)), including condensation, cloud droplet evaporation, the cloud droplet riming/freezing sink, and cloud-water advection/storage. Panels in the left column are averaged over the primary-rainband development stage (21:00 UTC 10 May–05:00 UTC 11 May), and panels in the right column over the later organizational adjustment stage (05:00–12:00 UTC 11 May). Unit: kg m^{-2} h^{-1}.

Local cores respond more strongly to aerosols than the regional mean (Fig. 10). During development, ΔRgen in 025 and AVE increases by 10.59 and 11.90 kg m^{-2} h^{-1}, respectively. The decomposition shows that the 025 enhancement is dominated by warm-rain generation, with a slight negative cold-rain anomaly, whereas AVE shows concurrent strengthening of warm- and cold-rain generation. In 075, ΔRgen turns negative at 3.53 kg m^{-2} h^{-1}, while ΔRadv increases by 6.72 kg m^{-2} h^{-1}; in MAX, ΔRgen decreases to −4.17 kg m^{-2} h^{-1} and ΔRadv increases by 2.90 kg m^{-2} h^{-1}. Above the AVE level, core precipitation becomes more dependent on external raindrop input or hydrometeor redistribution, and in situ raindrop generation no longer dominates. The adjustment stage further distinguishes sustained enhancement from local recovery. In 025, the source-term decomposition gives ΔRgen of +3.55 kg m^{-2} h^{-1}, with ΔRwarm decreasing by 4.03 kg m^{-2} h^{-1} and ΔRcold increasing by 7.58 kg m^{-2} h^{-1}. In AVE, ΔRgen is +16.22 kg m^{-2} h^{-1}, with ΔRwarm and ΔRcold increasing by 7.80 and 8.42 kg m^{-2} h^{-1}, respectively. In 075, ΔRgen is −8.74 kg m^{-2} h^{-1}, corresponding to ΔRwarm of −5.92 kg m^{-2} h^{-1} and ΔRcold of −3.32 kg m^{-2} h^{-1}. In MAX, ΔRgen recovers to +10.82 kg m^{-2} h^{-1}, with ΔRcold at +8.13 kg m^{-2} h^{-1}, exceeding ΔRwarm at +2.69 kg m^{-2} h^{-1}. The AVE core is still maintained jointly by warm and cold rain, whereas the MAX recovery relies mainly on cold rain and differs in both mechanism and spatial extent.

https://doi.org/10.5194/egusphere-2026-5128
Preprint. Discussion started: 29 September 2026

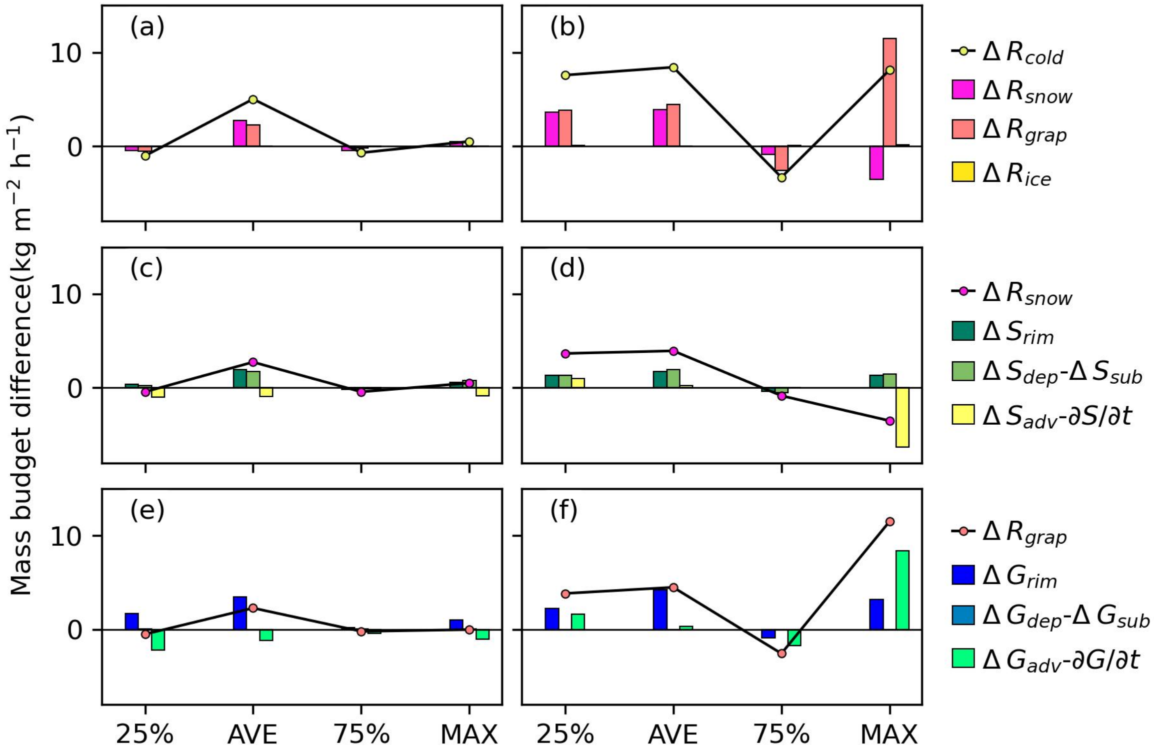

Figure 11: Aerosol impacts on the time-averaged cold-rain source budget within the representative convective-scale cores defined in Fig. S10, expressed as differences relative to the corresponding MIN core. (a, b) Differences in the total cold-rain source (ΔRcold) and its contributions from net conversion of ice crystals (ΔRice), snow (ΔRsnow), and graupel (ΔRgrap) to raindrops; (c, d) differences in the snow contribution (ΔRsnow) and the break-down terms of the snow mass-budget diagnostic (Eq. (10)), including riming (ΔSrim), net deposition minus sublimation (ΔSdep − ΔSsub), and lateral-advection/storage change (ΔSadv − Δ∂S/∂t); (e, f) differences in the graupel contribution (ΔRgrap) and the break-down terms of the graupel mass-budget diagnostic (Eq. (11)), including riming (ΔGrim), net deposition minus sublimation (ΔGdep − ΔGsub), and lateral-advection/storage change (ΔGadv − Δ∂G/∂t). Panels in the left column are averaged over the primary-rainband development stage (21:00 UTC 10 May–05:00 UTC 11 May), and panels in the right column over the later organizational adjustment stage (05:00–12:00 UTC 11 May). Unit: kg m^{-2} h^{-1}.

Cold-rain compensation is contributed mainly by snow and graupel processes, with late-stage MAX depending particularly on graupel transport and redistribution (Fig. 11). During development, ΔRcold in AVE increases by 5.03 kg m^{-2} h^{-1}, with snow, graupel, and ice crystals contributing 2.74, 2.27, and 0.02 kg m^{-2} h^{-1}, respectively; 075 decreases by 0.70 kg m^{-2} h^{-1}, while MAX increases by only 0.51 kg m^{-2} h^{-1}. During the adjustment stage, 025 and AVE increase by 7.58 and 8.42 kg m^{-2} h^{-1}, respectively, 075 decreases by 3.32 kg m^{-2} h^{-1}, and MAX turns to an increase of 8.13 kg m^{-2} h^{-1}. The net graupel-related contribution within the MAX core reaches 11.51 kg m^{-2} h^{-1}, dominated by advection and storage changes. This result is more consistent with a mechanism in which ice-phase hydrometeors are transported into local cores and then melt than with sustained enhancement of system-scale riming.

Fig. S10 and Figs. 10–11 reveal the scale difference in late-stage cold-rain enhancement in MAX: ΔRcold increases by 8.13 kg m^{-2} h^{-1} within the selected intense core, whereas the regionally averaged cold-rain component remains 0.07 kg m^{-2} h^{-1} lower than in MIN. Thus, late-stage cold-rain growth in MAX is concentrated mainly in a few intense cores and does not occur

https://doi.org/10.5194/egusphere-2026-5128
Preprint. Discussion started: 29 September 2026

broadly across the entire coastal rainband. This scale dependence further points to the role of the spatial configuration among thermodynamic perturbations, hydrometeor columns, and low-level inflow.

3.6 Effects of aerosols on thermodynamic–hydrometeor spatial coupling and low-level outflow configuration

To explain the contrast between the regional mean and local intense cores, we use the same core regions as those selected in Fig. S10. We compare the horizontal and vertical configurations of strong echoes, low-level winds, hydrometeor columns, and thermodynamic perturbations in Figs. 12–13, together with the buoyancy analysis in Fig. S11.

https://doi.org/10.5194/egusphere-2026-5128
Preprint. Discussion started: 29 September 2026

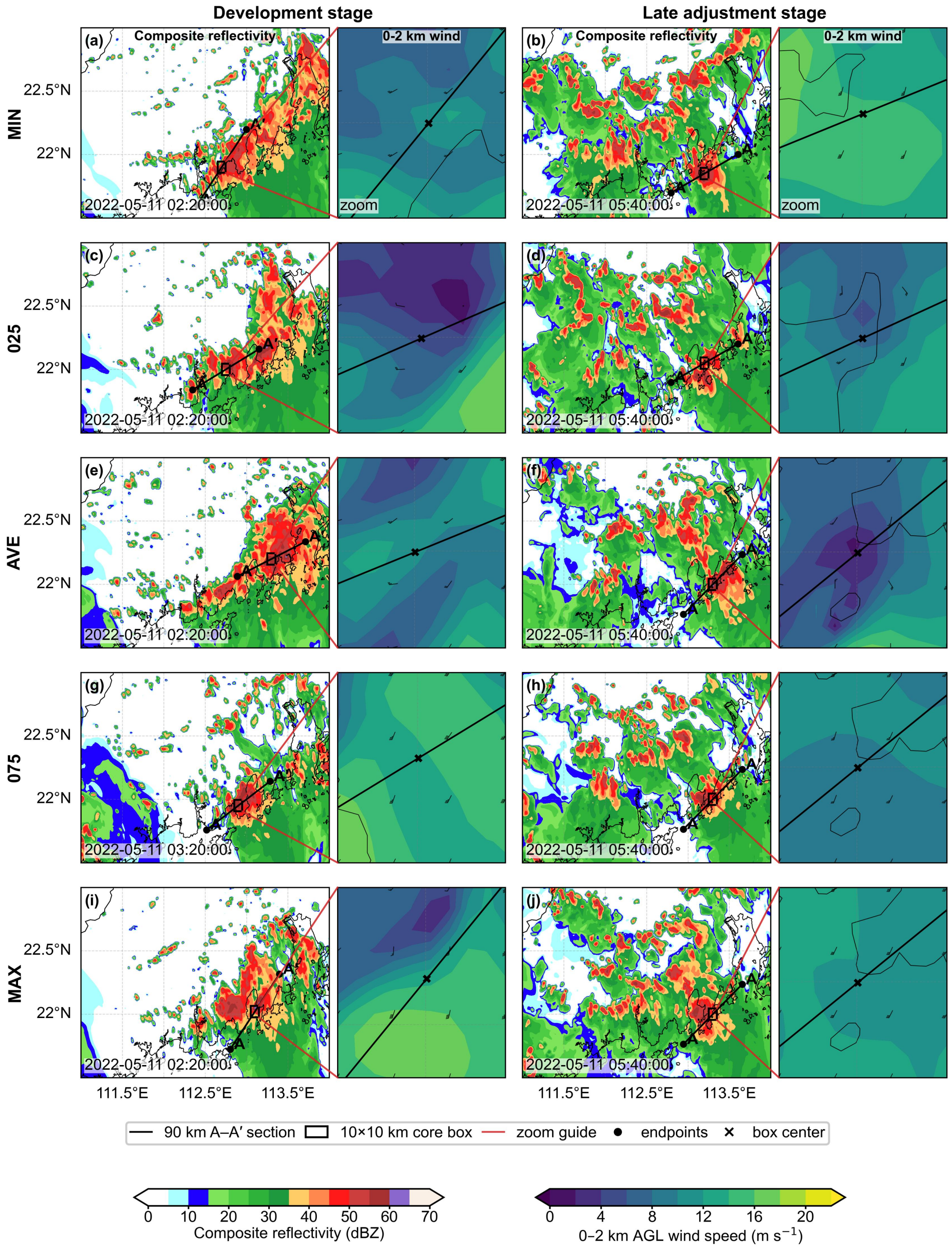

Figure 12: Cross-section locations and low-level wind-field configurations in convective-core regions under different aerosol backgrounds. Rows correspond to MIN, 025, AVE, 075, and MAX; the left and right groups show representative times in the

https://doi.org/10.5194/egusphere-2026-5128
Preprint. Discussion started: 29 September 2026

primary-rainband development stage and later organizational adjustment stage, respectively. Black lines indicate the A–A′ sections in Fig. 13, and red boxes indicate the 10 × 10 km core regions; wind-field panels show 0–2 km mean wind speed in the core region, and black crosses mark the core centers.

All experiments retain the primary coastal warm-sector rainband, but the spatial correspondence between strong-echo cores and low-level winds changes with aerosol concentration (Fig. 12). During development, as aerosol concentration increases from MIN through 025 to AVE, the along-coast strong echoes evolve from discontinuous to increasingly continuous, and the overlap between the cores and regions of high low-level wind speed also increases. In AVE, strong echoes are continuously aligned northeast–southwest, with the core embedded in the primary rainband; low-level supply, triggering locations, and mature precipitation cores are brought into closer alignment within the same regeneration band. With further increases to 075 and MAX, local strong echoes still occur, but the structure is more fragmented and the mismatch between high-wind regions and the cores increases. During the adjustment stage, AVE continues to maintain a concentrated, continuous coastal strong-echo band, whereas high reflectivity in 075 and MAX is mainly distributed in local clusters. This indicates that with further aerosol increases, newly initiated convection is more likely to deviate from the original primary rainband and develop in a dispersed manner.

https://doi.org/10.5194/egusphere-2026-5128
Preprint. Discussion started: 29 September 2026

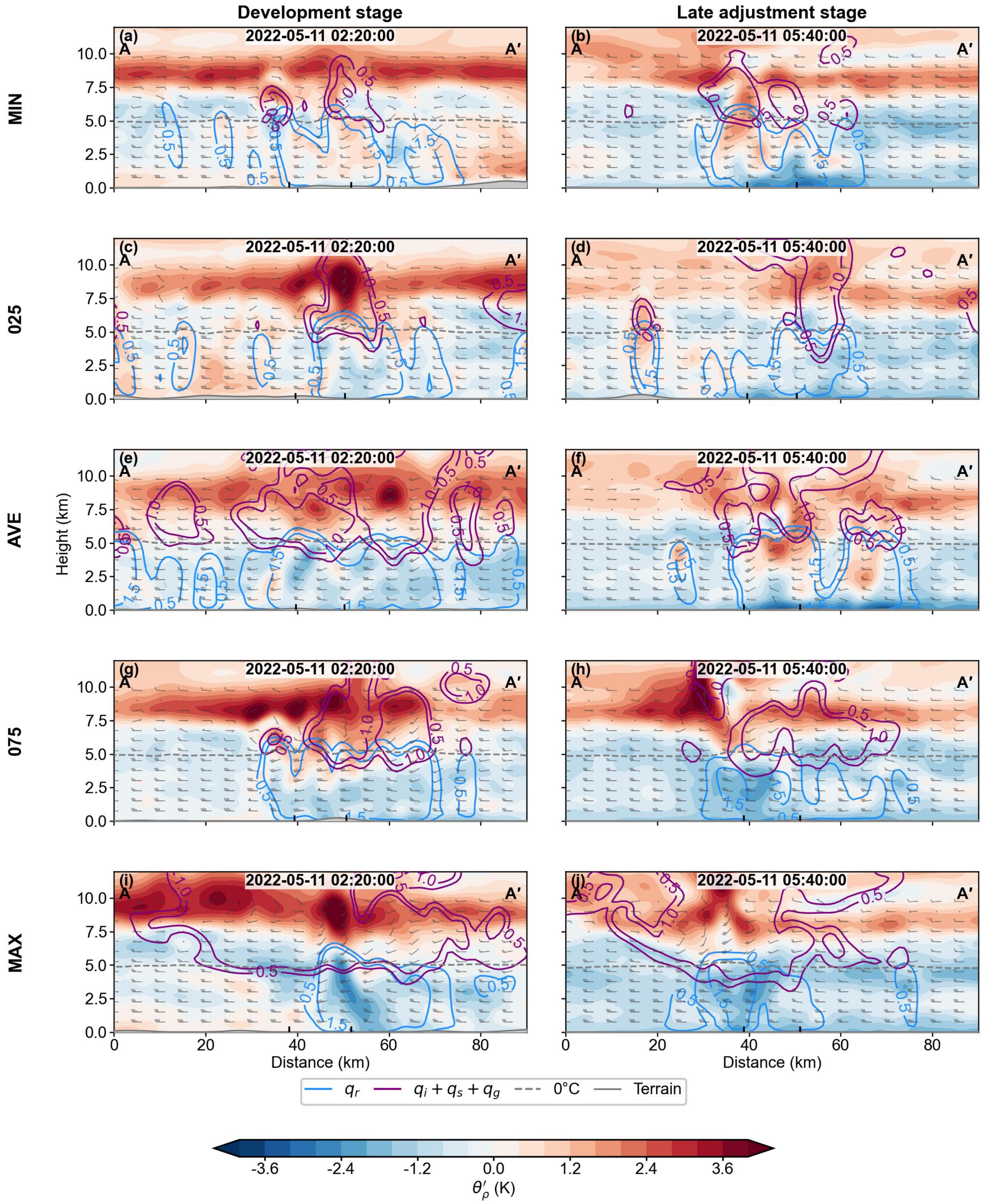

https://doi.org/10.5194/egusphere-2026-5128
Preprint. Discussion started: 29 September 2026

Figure 13: Thermodynamic–hydrometeor–circulation structures along the A–A′ cross sections at the representative times shown in Fig. 12. Panels (a, c, e, g, i) correspond to the development stage, and panels (b, d, f, h, j) correspond to the late adjustment stage. Rows from top to bottom represent the MIN, 025, AVE, 075, and MAX experiments, respectively. Shading denotes the density potential-temperature perturbation (θ'_{ρ}; K). Blue contours denote the rainwater mixing ratio (q_r), and purple contours denote the total ice-phase hydrometeor mixing ratio ($q_i + q_s + q_g$). The gray dashed line denotes the 0 °C level, and the gray solid line denotes terrain. Gray wind vectors show the combined horizontal wind component along the cross section and vertical velocity.

Representative cross sections show that the spatial coupling among hydrometeor columns, ascending motion, and thermodynamic perturbations first improves and then weakens as aerosol concentration increases (Fig. 13). Under low-concentration conditions, the high rainwater mixing ratios in MIN are located mainly below the 0 °C level, and ice-phase hydrometeors extend above the freezing level only locally; the vertical linkage among low-level rainwater, ice-phase hydrometeors, and ascent is weak. When aerosol concentration increases to 025, deeper hydrometeor columns begin to form in some convective cores and ice-phase hydrometeors develop into the middle and upper levels, but their persistent collocation with low-level cold anomalies, the main ascent region, and high-rainwater areas remains unstable. This indicates that although local deep convection and ice-phase growth have already appeared at low aerosol levels, the warm-rain supply, ice-phase conversion, and dynamical lifting have not yet become continuously connected.

As aerosol concentration increases further to AVE, the spatial correspondence between hydrometeors and dynamical structures improves markedly. During development, the area of high low-level rainwater values expands, and ice-phase hydrometeors develop continuously near and above the 0 °C level, broadly collocated with positive thermodynamic perturbations and stronger ascent in the middle and upper levels. Low-level rainwater, supercooled-water supply near the freezing level, and mid- to upper-level ice-phase hydrometeors occur within the same precipitation column, allowing condensational growth, collection of cloud water by raindrops, snow and graupel riming growth, and subsequent melting to become linked. This vertical structure is consistent with the system-scale budget results: as aerosol loading increases from low to moderate levels, the warm-rain process first establishes a stable water source, and ice-phase growth and melting then further increase rainwater generation. During the adjustment stage, AVE still maintains a clear vertical connection between rainwater and ice-phase hydrometeors; continuous ice-phase hydrometeors and centers of ascent overlie the low-level rainwater maximum, corresponding to the simultaneous strengthening of the warm- and cold-rain source terms in Fig. 10. Local intense cores can therefore remain structurally connected to the intermediate-scale primary rainband and support sustained along-coast convective regeneration.

When aerosol concentration increases further to 075 and MAX, local hydrometeor content does not decrease synchronously everywhere, but its spatial mismatch with the low-level dynamical structure becomes much more frequent. During development, ice-phase hydrometeors in 075 and MAX can still intensify above the 0 °C level and extend into the middle and upper troposphere or downstream; however, high low-level rainwater values, ice-phase hydrometeor columns, thermodynamic-perturbation centers, and the main ascent regions no longer remain stably collocated. Some ice-phase hydrometeors are transported outside the original convective cores, while the horizontal extent and vertical depth of low-level cold anomalies also increase. Under these conditions, local enhancement of ice-phase processes is less able to obtain a

https://doi.org/10.5194/egusphere-2026-5128
Preprint. Discussion started: 29 September 2026

sustained low-level warm-rain supply, so hydrometeor growth and melting are more likely to appear as dispersed local compensation rather than coordinated growth within a continuous precipitation column.

During the adjustment stage, this scale difference is most pronounced in MAX. MAX can exhibit local maxima of both rainwater and ice-phase hydrometeors, and the cold-rain source within the selected intense core is also clearly enhanced; however, the graupel-related budget is controlled mainly by advection and storage changes, indicating an important role for the transport and redistribution of ice-phase hydrometeors. Meanwhile, the connection of this local intense core with continuous low-level inflow, the main-rainband ascent region, and the intermediate-scale hydrometeor band is weaker than in AVE. Consequently, late-stage cold-rain enhancement in MAX is concentrated mainly in a few intense cores and does not indicate that in situ rainwater generation has recovered throughout the entire coastal rainband. This is consistent with the system-scale cold-rain contribution remaining near neutral and regionally averaged rainwater generation remaining below MIN.

Figures 12 and 13 together with Fig. S11 show that the dynamical influence of aerosols depends not only on the individual magnitudes of ascent, cold anomalies, or hydrometeor loading, but more importantly on the spatial configuration among these elements. As aerosol concentration increases from low to moderate levels, the enhanced warm-rain supply, ice-phase growth, low-level inflow, and primary ascent region increasingly overlap within the same precipitation band, allowing regionally averaged rainwater generation to be converted into continuous intermediate-scale regeneration. With further increases in concentration, mean cloud droplet size decreases and warm-rain formation and in situ rainwater generation are suppressed; at the same time, evaporative cooling and redistribution of hydrometeor loading strengthen low-level cold anomalies, increasing the influence of cold-pool outflow on convective triggering locations.

https://doi.org/10.5194/egusphere-2026-5128
Preprint. Discussion started: 29 September 2026

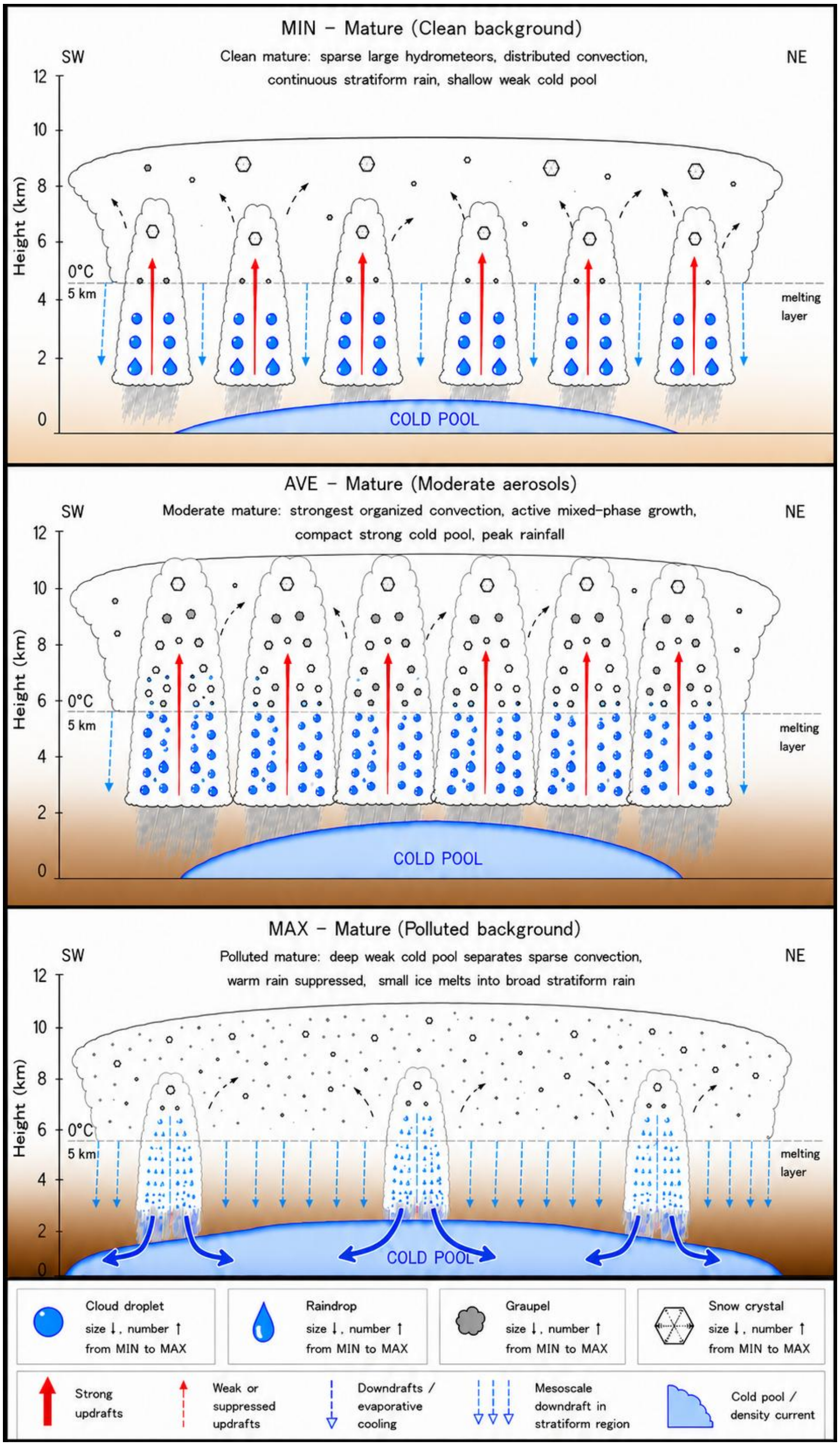

600 **Figure 14: Conceptual model of coastal warm-sector MCSs under clean, moderate, and high aerosol backgrounds. The three rows correspond to the clean background (MIN), moderate aerosol background (AVE), and high aerosol background (MAX), respectively.**

https://doi.org/10.5194/egusphere-2026-5128
Preprint. Discussion started: 29 September 2026

MIN is characterized by insufficient CCN, weak rainwater generation, and loosely separated convective clusters; AVE shows better coupling among warm-rain processes, riming/melting, and low-level supply, forming the most continuous linear MCS; MAX is dominated by small cloud droplets, suppressed warm rain, ice-phase hydrometeors spreading into the middle and upper levels, and widespread but weakly coupled cold anomalies, making the rainband more prone to fragmentation. Symbol meanings are given in the common legend.

4 Summary and discussion

Using the WRF model and the Thompson aerosol-aware microphysics scheme, this study performs five sensitivity experiments with different water-friendly aerosol concentrations for a warm-sector extreme-rainfall event over coastal South China on 10–11 May 2022. The results show that aerosols do not alter the double-rainband background maintained by large-scale circulation and moisture transport, but instead modulate coastal MCS precipitation non-monotonically through interactions among microphysical processes, dynamical feedbacks, and convective organization. As aerosol concentration rises from low to moderate levels, condensational growth and cloud-water collection by raindrops strengthen, while snow and graupel riming and melting further increase rainwater generation. The spatial correspondence among low-level inflow, ascent, and hydrometeor columns also improves, favoring sustained linkage among convective elements. With further increases in concentration, cloud droplet size decreases, warm-rain generation weakens, and low-level cold anomalies and outflow effects intensify. Although late-stage ice-phase compensation can restore a few intense cores, it does not restore system-scale rainwater generation or rainband continuity. Aerosol effects therefore arise from complex coupling among microphysical conversion, cold-pool feedbacks, and MCS organizational evolution.

The classical aerosol-invigoration hypothesis proposes that when warm rain is suppressed, more liquid water can be transported above the freezing level, where ice-phase growth and latent-heat release may strengthen deep convection (Khain et al., 2005; Lebo and Seinfeld, 2011). This pathway, however, depends strongly on environmental humidity, wind shear, and the state of convective organization (Igel and van den Heever, 2021). Condensation heating can also be offset by hydrometeor loading, entrainment, and precipitation fallout (Grabowski and Morrison, 2021). Observations and multimodel studies likewise show that updraft enhancement is not universal and that its magnitude depends strongly on both the model and the environment (Marinescu et al., 2021; Romps et al., 2023; Varble et al., 2023; Fan et al., 2025). The low-to-moderate part of this response is conceptually consistent with the aerosol-limited framework for warm convective clouds, in which insufficient CCN can constrain cloud development at very low aerosol concentrations (Koren et al., 2014). Our results show that the precipitation enhancement under moderate aerosol loading does not depend on any single process. Condensational growth and cloud-water collection by raindrops first provide a liquid-water source, after which snow and graupel riming and melting increase precipitation production, consistent with previous modeling that identified riming and melting as important pathways through which aerosol perturbations alter deep-convective precipitation (Cui et al., 2011). The coordination of a few controlling processes ultimately determines the net response.

Enhanced local ascent or cold-rain source terms do not necessarily translate into an increase in total precipitation. The buoyancy response is jointly controlled by latent-heat release, hydrometeor loading, and entrainment (Grabowski and Morrison,

https://doi.org/10.5194/egusphere-2026-5128
Preprint. Discussion started: 29 September 2026

2021). In this study, increased cold rain in intense cores late in MAX coexists with weak regionally averaged rainwater generation. This shows that whether an MCS is invigorated cannot be judged solely from local updrafts, radar reflectivity, or a single ice-phase process; generation efficiency, spatial extent, and duration must also be considered. Previous studies have reported a non-monotonic relationship in which precipitation first increases and then decreases with aerosol loading in convective clouds (Jiang et al., 2016; Lee and Feingold, 2010; Liu et al., 2019). Here, 2D-DCT confirms that the system-scale framework remains relatively stable, while MCE tracking distinguishes a continuous rainband from discrete clusters with high spectral power. As aerosol loading increases from low to moderate levels, medium and large elements remain connected; with further increases, elements either decay earlier or reappear later as dispersed cores. The precipitation transition therefore involves both changes in microphysical efficiency and an organizational shift in the convective regeneration chain.

Cold-pool feedbacks may connect the microphysical transition to organizational fragmentation. Previous studies have shown that CCN can alter the timing and intensity of cold-pool formation, although the response is constrained by environmental dry layers, wind shear, and storm structure (Grant and van den Heever, 2015; Chen et al., 2020; Ross and Lasher-Trapp, 2024). Rather than using cold-pool intensity alone to explain precipitation increases or decreases, this study focuses on the phase relationship among the cold-pool edge, low-level jet, newly initiated cells, and the mature rainband. Under moderate aerosol loading, the warm-rain water source, ice-phase growth, low-level supply, and main ascent region are well connected within the same precipitation column. Under high aerosol loading, warm rain weakens, cold anomalies expand, and mismatches between hydrometeor columns and the main ascent region become more frequent. Newly initiated convection is more likely to be triggered near the cold-pool edge, outside the rainband, or downstream, and progressively separates from mature precipitation cores. Cold pools may therefore alter not only convective intensity but also regeneration location. This positional effect explains why strong convection and ice-phase compensation can still occur late under high aerosol loading without rebuilding a continuous linear organization.

Several limitations should be noted. The five discrete-concentration experiments can identify only an approximate transition range, and AVE should not be regarded as a universal threshold. The transition point may vary with moisture, instability, vertical wind shear, and aerosol type. In particular, the present experiments perturb only water-friendly aerosols, whereas different aerosol types can produce distinct precipitation responses in deep convective clouds (Han et al., 2022). The Thompson aerosol-aware scheme represents only one microphysical formulation, and assumptions concerning the cloud droplet spectrum and scheme structure can also affect the simulated response (Marinescu et al., 2021; Zhang et al., 2021; Barthlott et al., 2022). In addition, cold-pool depth, outflow boundaries, and locations of convective initiation are diagnosed primarily from model output, and representative cross sections alone are insufficient to establish the full causal chain. Future work should combine multi-case ensemble simulations with multisource observations to test whether warm-rain establishment, cold-rain amplification, outward shifts in convective initiation, and organizational fragmentation are robust responses of coastal warm-sector MCSs in South China. Such analyses should also distinguish the relative contributions of microphysical perturbations, environmental covariability, and radiative effects.

Code and data availability

ERA5 hourly pressure-level and single-level reanalysis data used for the WRF initial and boundary conditions are openly available from the Copernicus Climate Change Service (C3S) Climate Data Store at https://cds.climate.copernicus.eu/datasets/reanalysis-era5-pressure-levels (https://doi.org/10.24381/cds.bd0915c6) and https://cds.climate.copernicus.eu/datasets/reanalysis-era5-single-levels (https://doi.org/10.24381/cds.adbb2d47), respectively. The CAMS global reanalysis (EAC4) monthly averaged fields used to construct the aerosol initial fields are openly available from the Copernicus Atmosphere Monitoring Service (CAMS) Atmosphere Data Store at https://ads.atmosphere.copernicus.eu/datasets/cams-global-reanalysis-eac4-monthly (https://doi.org/10.24381/fd75fff2). The ERA5 and CAMS EAC4 datasets are distributed under the applicable Copernicus data-store licences.

Author contributions

NT (Nuofeng Tan): conceptualization, formal analysis, investigation, and writing – original draft. PZ (Pengguo Zhao): conceptualization, methodology, supervision, and writing – review and editing. HX (Hui Xiao): resources, project administration, funding acquisition, and supervision. CZ (Chuanhong Zhao): data curation, validation, visualization, and writing – review and editing.

Competing interests

The authors declare that they have no conflict of interest.

Disclaimer

Copernicus Publications adds a standard disclaimer: "Copernicus Publications remains neutral with regard to jurisdictional claims made in the text, published maps, institutional affiliations, or any other geographical representation in this paper. While Copernicus Publications makes every effort to include appropriate place names, the final responsibility lies with the authors. Views expressed in the text are those of the authors and do not necessarily reflect the views of the publisher."

Acknowledgements

The authors acknowledge the Guangzhou Institute of Tropical and Marine Meteorology, China Meteorological Administration, for providing the high-performance computing resources and the observational data used in this study. The ERA5 reanalysis data were obtained from the Copernicus Climate Change Service (C3S), and the CAMS global reanalysis (EAC4) data were

https://doi.org/10.5194/egusphere-2026-5128
Preprint. Discussion started: 29 September 2026

obtained from the Copernicus Atmosphere Monitoring Service (CAMS). The authors are grateful for the open data policies of these providers.

Financial support

This work was supported by the National Natural Science Foundation of China (42475104), the Project of the Scientific and Technological Innovation Capacity Improvement Program of Chengdu University of Information Technology (KYTD202504), the Guangdong Basic and Applied Basic Research Foundation (2025A1515140056), and the Key Innovation Team of Guangdong Meteorological Bureau (GRMCTD202506-ZD06).

Review statement

The review statement will be added by Copernicus Publications listing the handling editor as well as all contributing referees according to their status anonymous or identified.

References

Albrecht, B. A.: Aerosols, cloud microphysics, and fractional cloudiness, Science, 245, 1227–1230, https://doi.org/10.1126/science.245.4923.1227, 1989.

Barthlott, C., Zarboo, A., Matsunobu, T., and Keil, C.: Importance of aerosols and shape of the cloud droplet size distribution for convective clouds and precipitation, Atmos. Chem. Phys., 22, 2153–2172, https://doi.org/10.5194/acp-22-2153-2022, 2022.

Bei, N., Xiao, B., Wang, R., Yang, Y., Liu, L., Han, Y., and Li, G.: Impacts of aerosol–radiation and aerosol–cloud interactions on a short-term heavy-rainfall event – a case study in the Guanzhong Basin, China, Atmos. Chem. Phys., 25, 10931–10948, https://doi.org/10.5194/acp-25-10931-2025, 2025.

Chen, Q., Fan, J., Yin, Y., and Han, B.: Aerosol impacts on mesoscale convective systems forming under different vertical wind shear conditions, J. Geophys. Res.-Atmos., 125, e2018JD030027, https://doi.org/10.1029/2018JD030027, 2020.

Cheng, C.-T., Wang, W.-C., and Chen, J.-P.: Simulation of the effects of increasing cloud condensation nuclei on mixed-phase clouds and precipitation of a front system, Atmos. Res., 96, 461–476, https://doi.org/10.1016/j.atmosres.2010.02.005, 2010.

Chin, M., Ginoux, P., Kinne, S., Torres, O., Holben, B. N., Duncan, B. N., Martin, R. V., Logan, J. A., Higurashi, A., and Nakajima, T.: Tropospheric aerosol optical thickness from the GOCART model and comparisons with sa

https://doi.org/10.5194/egusphere-2026-5128
Preprint. Discussion started: 29 September 2026

tellite and sun photometer measurements, J. Atmos. Sci., 59, 461–483, https://doi.org/10.1175/1520-0469(2002)059<0461:TAOTFT>2.0.CO;2, 2002.

Copernicus Atmosphere Monitoring Service (CAMS): CAMS global reanalysis (EAC4) monthly averaged fields, Atmosphere Data Store [data set], https://doi.org/10.24381/fd75fff2, 2020.

Copernicus Climate Change Service (C3S): ERA5 hourly data on pressure levels from 1940 to present, Climate Data Store [data set], https://doi.org/10.24381/cds.bd0915c6, 2018.

Copernicus Climate Change Service (C3S): ERA5 hourly data on single levels from 1940 to present, Climate Data Store [data set], https://doi.org/10.24381/cds.adbb2d47, 2018.

Cui, Z., Davies, S., Carslaw, K. S., and Blyth, A. M.: The response of precipitation to aerosol through riming and melting in deep convective clouds, Atmos. Chem. Phys., 11, 3495–3510, https://doi.org/10.5194/acp-11-3495-2011, 2011.

Davis, C. A., Brown, B. G., and Bullock, R.: Object-based verification of precipitation forecasts. Part I: Methodology and application to mesoscale rain areas, Mon. Weather Rev., 134, 1772–1784, https://doi.org/10.1175/MWR3145.1, 2006.

Denis, B., Côté, J., and Laprise, R.: Spectral decomposition of two-dimensional atmospheric fields on limited-area domains using the discrete cosine transform (DCT), Mon. Weather Rev., 130, 1812–1829, https://doi.org/10.1175/1520-0493(2002)130<1812:SDOTDA>2.0.CO;2, 2002.

Dixon, M. and Wiener, G.: TITAN: Thunderstorm identification, tracking, analysis, and nowcasting—A radar-based methodology, J. Atmos. Ocean. Technol., 10, 785–797, https://doi.org/10.1175/1520-0426(1993)010<0785:TTITAA>2.0.CO;2, 1993.

Fan, J., Yuan, T., Comstock, J. M., Ghan, S., Khain, A., Leung, L. R., Li, Z., Martins, V. J., and Ovchinnikov, M.: Dominant role by vertical wind shear in regulating aerosol effects on deep convective clouds, J. Geophys. Res.-Atmos., 114, D22206, https://doi.org/10.1029/2009JD012352, 2009.

Fan, J., Rosenfeld, D., Ding, Y., Leung, L. R., and Li, Z.: Potential aerosol indirect effects on atmospheric circulation and radiative forcing through deep convection, Geophys. Res. Lett., 39, L09806, https://doi.org/10.1029/2012GL051851, 2012.

Fan, J., Han, B., Varble, A., Morrison, H., North, K., Kollias, P., Chen, B., Dong, X., Giangrande, S. E., Khain, A., Lin, Y., Mansell, E., Milbrandt, J. A., Stenz, R., Thompson, G., and Wang, Y.: Cloud-resolving model intercomparison of an MC3E squall line case: Part I—Convective updrafts, J. Geophys. Res.-Atmos., 122, 9351–9378, https://doi.org/10.1002/2017JD026622, 2017.

Fan, J., Rosenfeld, D., Zhang, Y., Giangrande, S. E., Li, Z., Machado, L. A. T., Martin, S. T., Yang, Y., Wang, J., Artaxo, P., Barbosa, H. M. J., Braga, R. C., Comstock, J. M., Feng, Z., Gao, W., Gomes, H. B., Mei, F., Pöhlker, C., Pöhlker, M. L., Pöschl, U., and de Souza, R. A. F.: Substantial convection and precipitation enhancements by ultrafine aerosol particles, Science, 359, 411–418, https://doi.org/10.1126/science.aan8461, 2018.

https://doi.org/10.5194/egusphere-2026-5128
Preprint. Discussion started: 29 September 2026

Fan, J., Zhang, Y., Li, Z., Yan, H., Prabhakaran, T., Rosenfeld, D., and Khain, A.: Unveiling aerosol impacts on deep convective clouds: Scientific concept, modeling, observational analysis, and future direction, J. Geophys. Res.-Atmos., 130, e2024JD041931, https://doi.org/10.1029/2024JD041931, 2025.

Gao, W., Xue, L., Liu, L., Lu, C., Yun, Y., and Zhou, W.: A study of the fraction of warm rain in a pre-summer rainfall event over South China, Atmos. Res., 262, 105792, https://doi.org/10.1016/j.atmosres.2021.105792, 2021.

Grabowski, W. W. and Morrison, H.: Supersaturation, buoyancy, and deep convection dynamics, Atmos. Chem. Phys., 21, 13997–14018, https://doi.org/10.5194/acp-21-13997-2021, 2021.

Grant, L. D. and van den Heever, S. C.: Cold pool and precipitation responses to aerosol loading: Modulation by dry layers, J. Atmos. Sci., 72, 1398–1408, https://doi.org/10.1175/JAS-D-14-0260.1, 2015.

Guo, C., Chen, D., Chen, M., Zhang, S., Guo, J., and Ma, Z.: Aerosol impacts on summer precipitation forecast over the North China Plain by using Thompson aerosol-aware scheme in WRF: Statistical analysis and significant threat score improvements in polluted condition during June to August 2018, Atmos. Res., 299, 107177, https://doi.org/10.1016/j.atmosres.2023.107177, 2024.

Han, X., Zhao, B., Lin, Y., Chen, Q., Shi, H., Jiang, Z., Fan, X., Wang, J., Liou, K.-N., and Gu, Y.: Type-dependent impact of aerosols on precipitation associated with deep convective cloud over East Asia, J. Geophys. Res.-Atmos., 127, e2021JD036127, https://doi.org/10.1029/2021JD036127, 2022.

Hersbach, H., Bell, B., Berrisford, P., Hirahara, S., Horányi, A., Muñoz-Sabater, J., Nicolas, J., Peubey, C., Radu, R., Schepers, D., Simmons, A., Soci, C., Abdalla, S., Abellan, X., Balsamo, G., Bechtold, P., Biavati, G., Bidlot, J., Bonavita, M., De Chiara, G., Dahlgren, P., Dee, D., Diamantakis, M., Dragani, R., Flemming, J., Forbes, R., Fuentes, M., Geer, A., Haimberger, L., Healy, S., Hogan, R. J., Hólm, E., Janisková, M., Keeley, S., Laloyaux, P., Lopez, P., Lupu, C., Radnoti, G., de Rosnay, P., Rozum, I., Vamborg, F., Villaume, S., and Thépaut, J.-N.: The ERA5 global reanalysis, Q. J. Roy. Meteor. Soc., 146, 1999–2049, https://doi.org/10.1002/qj.3803, 2020.

Houze Jr., R. A.: Mesoscale convective systems, Rev. Geophys., 42, RG4003, https://doi.org/10.1029/2004RG000150, 2004.

Iacono, M. J., Delamere, S. J., Mlawer, E. J., Shephard, M. W., Clough, S. A., and Collins, W. D.: Radiative forcing by long-lived greenhouse gases: Calculations with the AER radiative transfer models, J. Geophys. Res.-Atmos., 113, D13103, https://doi.org/10.1029/2008JD009944, 2008.

Igel, A. L. and van den Heever, S. C.: Invigoration or enervation of convective clouds by aerosols? Geophys. Res. Lett., 48, e2021GL093804, https://doi.org/10.1029/2021GL093804, 2021.

Inness, A., Ades, M., Agustí-Panareda, A., Barré, J., Benedictow, A., Blechschmidt, A.-M., Dominguez, J. J., Engelen, R., Eskes, H., Flemming, J., Huijnen, V., Jones, L., Kipling, Z., Massart, S., Parrington, M., Peuch, V.-H., Razinger, M., Remy, S., Schulz, M., and Suttie, M.: The CAMS reanalysis of atmospheric composition, Atmos. Chem. Phys., 19, 3515–3556, https://doi.org/10.5194/acp-19-3515-2019, 2019.

https://doi.org/10.5194/egusphere-2026-5128
Preprint. Discussion started: 29 September 2026

Jiang, M., Li, Z., Wan, B., and Cribb, M.: Impact of aerosols on precipitation from deep convective clouds in eastern China, J. Geophys. Res.-Atmos., 121, 9607–9620, https://doi.org/10.1002/2015JD024246, 2016.

Khain, A., Rosenfeld, D., and Pokrovsky, A.: Aerosol impact on the dynamics and microphysics of deep convective clouds, Q. J. Roy. Meteor. Soc., 131, 2639–2663, https://doi.org/10.1256/qj.04.62, 2005.

Khain, A. P.: Notes on state-of-the-art investigations of aerosol effects on precipitation: A critical review, Environ. Res. Lett., 4, 015004, https://doi.org/10.1088/1748-9326/4/1/015004, 2009.

Khain, A., Lynn, B., and Dudhia, J.: Aerosol effects on intensity of landfalling hurricanes as seen from simulations with the WRF model with spectral bin microphysics, J. Atmos. Sci., 67, 365–384, https://doi.org/10.1175/2009JAS3210.1, 2010.

Koren, I., Dagan, G., and Altaratz, O.: From aerosol-limited to invigoration of warm convective clouds, Science, 344, 1143–1146, https://doi.org/10.1126/science.1252595, 2014.

Lebo, Z. J. and Seinfeld, J. H.: Theoretical basis for convective invigoration due to increased aerosol concentration, Atmos. Chem. Phys., 11, 5407–5429, https://doi.org/10.5194/acp-11-5407-2011, 2011.

Lee, S.-S. and Feingold, G.: Precipitating cloud-system response to aerosol perturbations, Geophys. Res. Lett., 37, L23806, https://doi.org/10.1029/2010GL045596, 2010.

Li, Z., Niu, F., Fan, J., Liu, Y., Rosenfeld, D., and Ding, Y.: Long-term impacts of aerosols on the vertical development of clouds and precipitation, Nat. Geosci., 4, 888–894, https://doi.org/10.1038/ngeo1313, 2011.

Lin, Y. and Zhang, F.: Tracking gravity waves in baroclinic jet-front systems, J. Atmos. Sci., 65, 2402–2415, https://doi.org/10.1175/2007JAS2482.1, 2008.

Liu, H., Guo, J., Koren, I., Altaratz, O., Dagan, G., Wang, Y., Jiang, J. H., Zhai, P., and Yung, Y. L.: Non-monotonic aerosol effect on precipitation in convective clouds over tropical oceans, Sci. Rep., 9, 7809, https://doi.org/10.1038/s41598-019-44284-2, 2019.

Luo, Y., Xia, R., and Chan, J. C. L.: Characteristics, physical mechanisms, and prediction of pre-summer rainfall over South China: research progress during 2008–2019, J. Meteorol. Soc. Jpn., 98, 19–42, https://doi.org/10.2151/jmsj.2020-002, 2020.

Marinescu, P. J., van den Heever, S. C., Heikenfeld, M., Barrett, A. I., Barthlott, C., Hoose, C., Fan, J., Fridlind, A. M., Matsui, T., Miltenberger, A. K., Stier, P., Vie, B., White, B. A., and Zhang, Y.: Impacts of varying concentrations of cloud condensation nuclei on deep convective cloud updrafts: A multimodel assessment, J. Atmos. Sci., 78, 1147–1172, https://doi.org/10.1175/JAS-D-20-0200.1, 2021.

Morrison, H. and Grabowski, W. W.: Cloud-system resolving model simulations of aerosol indirect effects on tropical deep convection and its thermodynamic environment, Atmos. Chem. Phys., 11, 10503–10523, https://doi.org/10.5194/acp-11-10503-2011, 2011.

https://doi.org/10.5194/egusphere-2026-5128
Preprint. Discussion started: 29 September 2026

Romps, D. M., Latimer, K., Zhu, Q., Jurkat-Witschas, T., Mahnke, C., Prabhakaran, T., Weigel, R., and Wendisch, M.: Air pollution unable to intensify storms via warm-phase invigoration, Geophys. Res. Lett., 50, e2022GL100409, https://doi.org/10.1029/2022GL100409, 2023.

Rosenfeld, D., Lohmann, U., Raga, G. B., O'Dowd, C. D., Kulmala, M., Fuzzi, S., Reissell, A., and Andreae, M. O.: Flood or drought: How do aerosols affect precipitation?, Science, 321, 1309–1313, https://doi.org/10.1126/science.1160606, 2008.

Ross, T. I. D. and Lasher-Trapp, S.: On CCN effects upon convective cold pool timing and features, Mon. Weather Rev., 152, 891–906, https://doi.org/10.1175/MWR-D-23-0154.1, 2024.

Shin, H. H. and Hong, S.-Y.: Representation of the subgrid-scale turbulent transport in convective boundary layers at gray-zone resolutions, Mon. Weather Rev., 143, 250–271, https://doi.org/10.1175/MWR-D-14-00116.1, 2015.

Stier, P., van den Heever, S. C., Christensen, M. W., Gryspeerdt, E., Dagan, G., Saleeby, S. M., Bollasina, M., Donner, L., Emanuel, K., Ekman, A. M. L., Feingold, G., Field, P., Forster, P., Haywood, J., Kahn, R., Koren, I., Kummerow, C., L'Ecuyer, T., Lohmann, U., Ming, Y., Myhre, G., Quaas, J., Rosenfeld, D., Samset, B., Seifert, A., Stephens, G., and Tao, W.-K.: Multifaceted aerosol effects on precipitation, Nat. Geosci., 17, 719–732, https://doi.org/10.1038/s41561-024-01482-6, 2024.

Storer, R. L., van den Heever, S. C., and Stephens, G. L.: Modeling aerosol impacts on convective storms in different environments, J. Atmos. Sci., 67, 3904–3915, https://doi.org/10.1175/2010JAS3363.1, 2010.

Tewari, M., Chen, F., Wang, W., Dudhia, J., LeMone, M. A., Mitchell, K., Ek, M., Gayno, G., Wegiel, J., and Cuenca, R. H.: Implementation and verification of the unified Noah land surface model in the WRF model, 20th Conference on Weather Analysis and Forecasting/16th Conference on Numerical Weather Prediction, Seattle, WA, USA, 14 January 2004, Paper 14.2a, American Meteorological Society, 2004.

Thompson, G. and Eidhammer, T.: A study of aerosol impacts on clouds and precipitation development in a large winter cyclone, J. Atmos. Sci., 71, 3636–3658, https://doi.org/10.1175/JAS-D-13-0305.1, 2014.

Tonn, M., Barthlott, C., Kunz, M., and Hoose, C.: Impact of wind shear on aerosol–cloud interactions and convective precipitation, Front. Environ. Sci., 13, 1566365, https://doi.org/10.3389/fenvs.2025.1566365, 2025.

Twomey, S.: The influence of pollution on the shortwave albedo of clouds, J. Atmos. Sci., 34, 1149–1152, https://doi.org/10.1175/1520-0469(1977)034<1149:TIOPOT>2.0.CO;2, 1977.

Varble, A.: Erroneous attribution of deep convective invigoration to aerosol concentration, J. Atmos. Sci., 75, 1351–1368, https://doi.org/10.1175/JAS-D-17-0217.1, 2018.

Varble, A. C., Igel, A. L., Morrison, H., Grabowski, W. W., and Lebo, Z. J.: Opinion: A critical evaluation of the evidence for aerosol invigoration of deep convection, Atmos. Chem. Phys., 23, 13791–13808, https://doi.org/10.5194/acp-23-13791-2023, 2023.

https://doi.org/10.5194/egusphere-2026-5128
Preprint. Discussion started: 29 September 2026

Wang, Y., Zhang, Z., Chow, W. S., Wang, Z., Yu, J. Z., Fung, J. C.-H., and Shi, X.: Investigating the effect of aerosol uncertainty on convective precipitation forecasting in South China's coastal area, J. Geophys. Res.-Atmos., 128, e2023JD038694, https://doi.org/10.1029/2023JD038694, 2023.

Xia, F., Liu, X.-T., Hu, S., Li, H.-Q., Rao, X.-N., Lin, Q., Xiao, H., Feng, L., and Lai, R.-Z.: Comparison of microphysical characteristics of warm-sector, frontal and shear-line heavy rainfall during the pre-summer rainy season in South China, J. Trop. Meteorol., 29, 204–215, https://doi.org/10.46267/j.1006-8775.2023.016, 2023.

Xiao, H., Liu, X., Li, H., Yue, Q., Feng, L., and Qu, J.: Extent of aerosol effect on the precipitation of squall lines: A case study in South China, Atmos. Res., 292, 106886, https://doi.org/10.1016/j.atmosres.2023.106886, 2023.

Xiao, H., Hu, S., Liu, X., Li, H., He, S., and Feng, L.: Improvement of microphysics schemes for a warm-sector heavy precipitation over South China, Atmos. Res., 315, 107905, https://doi.org/10.1016/j.atmosres.2024.107905, 2025.

Zhang, C., Wang, Y., and Hamilton, K.: Improved representation of boundary layer clouds over the southeast Pacific in ARW-WRF using a modified Tiedtke cumulus parameterization scheme, Mon. Weather Rev., 139, 3489–3513, https://doi.org/10.1175/MWR-D-10-05091.1, 2011.

Zhang, Y., Fan, J., Li, Z., and Rosenfeld, D.: Impacts of cloud microphysics parameterizations on simulated aerosol–cloud interactions for deep convective clouds over Houston, Atmos. Chem. Phys., 21, 2363–2381, https://doi.org/10.5194/acp-21-2363-2021, 2021.